

## Article

# Effect of Graphene Oxide-Modified CaAl-Layered Double Hydroxides on the Carbon Dioxide Permeation Properties of Fluoroelastomers

Chuanbo Cong \*, Daigang Peng , Qingkun Liu, Mingyang Yuan, Xiaoyu Meng and Qiong Zhou

New Energy and Material College, China University of Petroleum, Beijing 102249, China; pengdg\_123@163.com (D.P.); liuqingkun1992@163.com (Q.L.); yuanmy.apply@gmail.com (M.Y.); xymeng800418@sohu.com (X.M.); zhouqiong\_cn@163.com (Q.Z.)

\* Correspondence: congcb@cup.edu.com

**Abstract:** This work aimed to investigate the CO<sub>2</sub> gas barrier and mechanical properties of fluorine rubber nanocomposites filled with Ca/Al layered hydroxide (graphene oxide [GO]/LDH-Ca<sub>2</sub>Al) modified by GO. GO/LDH-Ca<sub>2</sub>Al nanocomposite fillers were prepared by depositing Ca/Al layered hydroxide (LDH-Ca<sub>2</sub>Al) into the surface of alkalized GO (Al-GO). The prepared GO/LDH-Ca<sub>2</sub>Al nanocomposite fillers and complexes were characterized by Fourier infrared spectroscopy (FTIR), X-ray diffraction (XRD), scanning electron microscopy (SEM), and transmission electron microscopy (TEM) for structural and micromorphological characterization. The results showed that GO/LDH-Ca<sub>2</sub>Al was successfully prepared with strong interactions between Al-GO and LDH, and the compatibility of GO/LDH-Ca<sub>2</sub>Al nanocomposite fillers with the polymer was significantly improved compared with that of LDH-Ca<sub>2</sub>Al. Consequently, both the fracture strength ( $\sigma_b$ ) and strain ( $\varepsilon_b$ ) of GO/LDH-Ca<sub>2</sub>Al nanocomplexes remarkably increased, and they exhibited excellent mechanical properties. Differential scanning calorimetry and thermogravimetric analysis were used to characterize the thermal stability of GO/LDH-Ca<sub>2</sub>Al nanocomposite fillers, and GO/LDH-Ca<sub>2</sub>Al nanocomposite fillers have better thermal stability than LDH-Ca<sub>2</sub>Al. The reaction products (S-LDH-Ca<sub>2</sub>Al and S-GO-Ca<sub>2</sub>Al) of LDH-Ca<sub>2</sub>Al and GO/LDH-Ca<sub>2</sub>Al with CO<sub>2</sub> were characterized using XRD and TGA, respectively, and the results show that LDH-Ca<sub>2</sub>Al reacts readily and chemically with CO<sub>2</sub>, resulting in a lower diffusion coefficient of CO<sub>2</sub> in the LDH-Ca<sub>2</sub>Al nanocomplexes than that of the GO/LDH-Ca<sub>2</sub>Al nanocomplexes and leading to the destruction of the laminar structure of LDH-Ca<sub>2</sub>Al, while GO/LDH-Ca<sub>2</sub>Al has better CO<sub>2</sub> resistance stability. GO/LDH-Ca<sub>2</sub>Al nanocomplexes exhibited a reduced content of hydroxyl groups with pro-CO<sub>2</sub> nature exposed on the surface of LDH-Ca<sub>2</sub>Al, improving the interfacial interaction between the nanofillers and the rubber matrix and enhancing the dispersion of GO/LDH-Ca<sub>2</sub>Al in the polymers. Moreover, CO<sub>2</sub> in the soluble GO/LDH-Ca<sub>2</sub>Al nanocomposites was significantly reduced, while the diffusion properties demonstrated weak temperature dependence on solubility. The mechanism of the CO<sub>2</sub> gas barrier of polymers filled with GO/LDH-Ca<sub>2</sub>Al was proposed on the basis of the Arrhenius equation.

**Keywords:** LDH; graphene oxide; permeability; carbon dioxide



**Citation:** Cong, C.; Peng, D.; Liu, Q.; Yuan, M.; Meng, X.; Zhou, Q. Effect of Graphene Oxide-Modified CaAl-Layered Double Hydroxides on the Carbon Dioxide Permeation Properties of Fluoroelastomers. *Polymers* **2023**, *15*, 4151. <https://doi.org/10.3390/polym15204151>

Academic Editor: Fernão D. Magalhães

Received: 12 September 2023

Revised: 12 October 2023

Accepted: 16 October 2023

Published: 19 October 2023



**Copyright:** © 2023 by the authors. Licensee MDPI, Basel, Switzerland. This article is an open access article distributed under the terms and conditions of the Creative Commons Attribution (CC BY) license (<https://creativecommons.org/licenses/by/4.0/>).

## 1. Introduction

Climate change is one of the most serious problems facing mankind, and anthropogenic air pollutant emissions and climate change have a direct relationship in which carbon dioxide (CO<sub>2</sub>) is the main air pollutant [1]. In the field of oilfield development, CO<sub>2</sub> is an attractive repellent for enhanced oil recovery, but some problems, such as CO<sub>2</sub> leakage during CO<sub>2</sub> transportation, are encountered; hence, a sealing material with excellent barrier performance needs to be developed [2].

Rubber is a highly elastic and amorphous polymer with good toughness, elasticity, and elongation, and they are also known as elastomers; for this class of material, a very

small external force can produce a large deformation, which can be restored after removing the external force [3,4]. Rubber materials are widely used in tire liners, chemical protection products, medical packaging, automotive tanks and natural gas storage tanks, and natural long-distance pipeline valve sealing materials, and their gas barrier properties are very important [5]. The gas barrier properties of rubber materials are very important. Given the high free volume fraction between rubber molecular chains, gas molecules can easily diffuse from one end of the rubber material to the other, and most diene-based rubbers such as natural rubber (NR), ethylene-propylene rubber (EPDM), and styrene-butadiene rubber (SBR) have high permeability to gases [6].

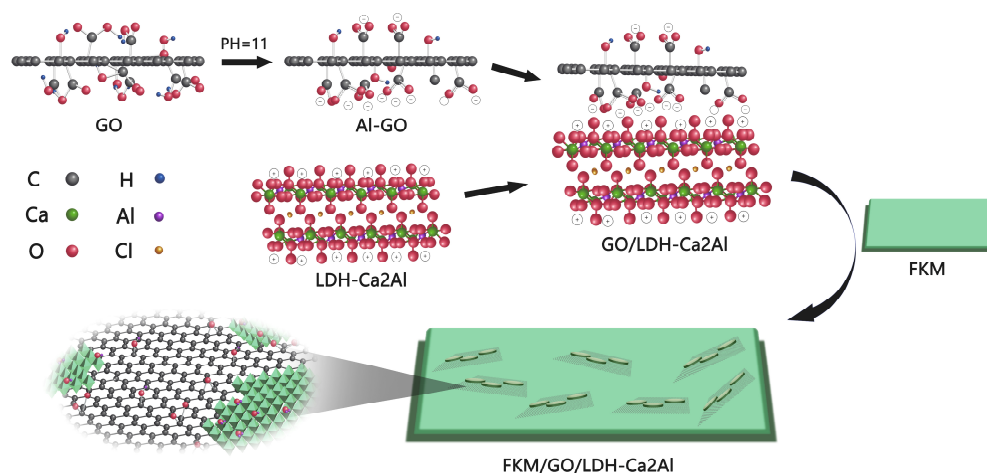
The gas barrier properties can be effectively improved by filling a certain amount of nanoparticles into the rubber to form a filling network, thus creating distorted paths and inhibiting gas molecules from penetrating the rubber matrix. More importantly, the strong interface between the nanoparticles and the rubber molecules is significant in limiting chain migration and further reducing the free volume between the nanoparticles and the rubber molecules. Among a range of nanoparticles, layered particles such as layered double hydroxides (LDH) [7–9] and graphene (GE) or graphene oxide (GO) [10,11] have higher aspect ratios than spherical and fibrous particles, making them more conducive to enhancing the gas barrier properties of rubber composites [12]. In particular, LDH is considered to be a promising CO<sub>2</sub> adsorbent because of its controllable layer spacing and pro-CO<sub>2</sub> properties [13]. The chemical formula of LDH can be represented by the general expression  $M_{1-x}^{2+}M_x^{3+}(\text{OH})_2(\text{A}^{n-})_{x/n}\cdot y\text{H}_2\text{O}$  [14,15]. LDH consists of a hydromagnesite-like layer in which a small portion of octahedrally coordinated divalent metal cations is replaced by trivalent metal cations, resulting in a positively charged host layer [16]. Exchangeable inorganic or organic anions are accommodated in the interlayer channels to compensate for the positive charge. In addition, the hydroxyl groups of the host layer are connected to anions or water molecules via hydrogen bonding. The X value is equal to the molar ratio of  $M^{3+}/(M^{2+}+M^{3+})$ , and it ranges from 0.17 to 0.33 [16]. Given the controllable  $M^{2+}/M^{3+}$  molar ratio, the tunability of the metal cations, and the exchangeable charge compensating anions [17], the layer spacing of the LDH can be optimized, which can aid in the design of the lamellar packing that facilitates CO<sub>2</sub> intercalation, further forming a more complex pathway for CO<sub>2</sub> diffusion.

However, the thermal stability of LDH is poor, and it starts to undergo layer structure destruction at approximately 250 °C [18]. Most importantly, LDH is a polar inorganic material with limited compatibility with organic macromolecules such as natural rubber (NR), fluorine rubber (FKM), and nitrile rubber (NBR), leading to agglomeration in the polymer and the formation of weak phase interfaces [8,9]. Therefore, the dispersion and thermal stability of LDH in polymers can be improved by forming a compound with LDH along with new components. GO has high electronic conductivity, good mechanical strength, excellent thermal stability, large specific area, and abundant oxygen-containing groups on its surface, such as epoxide, hydroxyl, and carboxyl groups, which can form strong interactions with polymer molecules via hydrogen or ionic bonding [13–15]. It also has good descriptive properties with polymers. Moreover, GO is an almost monolayer layered structure with a large surface area [19]. GO is an ideal carrier for LDH because of its negatively charged layer surface and oxygen-containing groups, which can form hydrogen bonding and strong electrostatic interactions with the positively charged LDH on the surface of the host layer [20–22]. Yang et al. prepared FeNi-LDH/GO hybrid nanosheets by alternately stacking GO layers and FeNi double hydroxide ion layers [20].

To meet the application requirements for rubber of the tire, aerospace, and military fields, nanofillers such as graphene oxide, carbon nanotubes, carbon black, and montmorillonite have been widely used to improve the mechanical properties of rubber. The effects of various modifying additives and fillers on the physicochemical and mechanical properties of polymer composites are determined by many factors as follows: (1) filler–polymer interfacial interaction [23–25], (2) content of fillers [26], and (3) cross-linking density of

polymers [27]. Among these, filler–polymer interfacial interaction exerts an extremely significant effect on the mechanical properties of polymer composites.

In this study, GO/LDH- $\text{Ca}_2\text{Al}$  nanolamellar fillers with better thermal stability and better compatibility with polymers were prepared via a simple synthesis method (Scheme 1). The layer spacing of this nanofiller increased by approximately 0.04 nm compared with that of pristine LDH- $\text{Ca}_2\text{Al}$ , thus increasing the chances of interlayer insertion of  $\text{CO}_2$  gas molecules. At the same time, the resistance to  $\text{CO}_2$  stability was significantly improved, and a stable layer structure can be maintained in a  $\text{CO}_2$  environment. The GO/LDH- $\text{Ca}_2\text{Al}$  nanofiller reduced the content of exposed hydroxyl groups of a pro- $\text{CO}_2$  nature on the surface of LDH- $\text{Ca}_2\text{Al}$ , increased the interfacial interactions between LDH- $\text{Ca}_2\text{Al}$  and the rubber matrix, and improved the dispersion of LDH- $\text{Ca}_2\text{Al}$  in the polymer. Consequently, the  $\text{CO}_2$  solubility of the nanocomposites was significantly reduced.



**Scheme 1.** Preparation flow of GO/LDH- $\text{Ca}_2\text{Al}$  nanocomposite fillers.

## 2. Experimental

### 2.1. Materials

FKM 246, a terpolymer of vinylidene fluoride (VF2); hexafluoropropylene (HFP); and tetrafluoroethylene (TFE), with 68.5% fluorine content, density of  $1.86 \text{ g/cm}^3$ , Mooney viscosity, ML 1 + 10 at  $121 \text{ }^\circ\text{C} = 25$ , and solubility parameter,  $\delta = 19.7 \text{ MPa}^{1/2}$  were supplied by Shanghai Huayi 3F New Materials Co., Ltd. (Shanghai, China). 2,5-Dimethyl-2,5-di(tert-butylperoxy)hexane (Macklin), triallyl isocyanurate (TAIC,  $\geq 98\%$ , Aladdin), and calcium chloride dihydrate ( $\text{CaCl}_2 \cdot 2\text{H}_2\text{O}$ ,  $\geq 98\%$ ) were purchased from Beijing Yongchang Haoran Bio-technology Co., Ltd. (Beijing, China). Aluminum chloride hexahydrate ( $\text{AlCl}_3 \cdot 6\text{H}_2\text{O}$ ,  $\geq 98\%$ ) was obtained from Shanghai Taitan Technology Co., Ltd. (Shanghai, China). Graphene oxide (GO,  $>99\%$ ), sodium hydroxide ( $\text{NaOH}$ ,  $\geq 98\%$ ), and deionized water were purchased from Shanghai Boer Chemical Reagent Co. (Shanghai, China). All reagents were of analytical grade, and the purity of the  $\text{CO}_2$  test gas used for the experiments was 99.9% (Beijing Chengweixin Industrial Gas Sales Center, Beijing, China).

### 2.2. Preparation of Layered LDH- $\text{Ca}_2\text{Al}$ and GO/LDH- $\text{Ca}_2\text{Al}$

LDH- $\text{Ca}_2\text{Al}$  was prepared via co-precipitation [28–30]. Approximately 15 g  $\text{CaCl}_2 \cdot 2\text{H}_2\text{O}$  and 7.606 g  $\text{AlCl}_3 \cdot 6\text{H}_2\text{O}$  were dissolved in 300 mL of deionized water to obtain a colorless and transparent  $\text{Ca}_2\text{Al}$  solution. Approximately 7.36 g  $\text{NaOH}$  was dissolved in 30 mL of deionized water to obtain a colorless and transparent  $\text{NaOH}$  solution, and the  $\text{NaOH}$  solution was added to the vigorously stirred (800 rpm)  $\text{Ca}_2\text{Al}$  solution at room temperature. The pH of the suspension was maintained at approximately 11, and stirring was maintained for 1 h. The sample was then filtered, washed with deionized water until the pH was approximately 10, and finally vacuum-dried at  $60 \text{ }^\circ\text{C}$  to obtain the white powder LDH- $\text{Ca}_2\text{Al}$ .

Approximately 0.5 g GO was added to 1050 mL of deionized water to obtain the GO suspension [31]. Then, an appropriate amount of NaOH was added to adjust the pH of GO suspension at approximately 11 (Al-GO), and 8.15 g LDH-Ca<sub>2</sub>Al was added to the solution. The sample was sonicated for 10 min and then placed in a vacuum oven at 60 °C for 24 h to obtain GO/LDH-Ca<sub>2</sub>Al suspension. Finally, it was filtered, washed with deionized water, and freeze-dried.

### 2.3. CO<sub>2</sub> Resistance Stability Testing of LDH-Ca<sub>2</sub>Al and GO/LDH-Ca<sub>2</sub>Al

S-LDH-Ca<sub>2</sub>Al and S-GO/LDH-Ca<sub>2</sub>Al, which were intercalated and reacted by CO<sub>2</sub>, were obtained by simultaneously placing 1.5 g of LDH-Ca<sub>2</sub>Al and GO/LDH-Ca<sub>2</sub>Al in an autoclave of CO<sub>2</sub> gas as the ambient medium at 80 °C and 4.3 MPa, and the sample was taken out after 1 day.

### 2.4. Preparation of FKM/GO/LDH-Ca<sub>2</sub>Al and FKM/LDH-Ca<sub>2</sub>Al Composites

The raw rubber was sheared on the rolls for 2 min at room temperature by using an open double-roller mill (friction ratio: 1:1.4). Then, different proportions of GO/LDH-Ca<sub>2</sub>Al were added for 3–4 min. Finally, 5 phr LUPEROX 101XL-50 and 5 phr TAIC were added to the sample, and the mixture was sheared and agitated for 3–4 min to obtain the unvulcanized FKM/GO/Ca<sub>2</sub>Al composite. A rotorless vulcanometer was used to determine the optimal vulcanization time (tc90) of the unvulcanized FKM/GO/LDH-Ca<sub>2</sub>Al composites at 160 °C, and was vulcanized to the optimal vulcanization time (tc90) by using a plate vulcanizer at 160 °C and 10 MPa. FKMs unfilled and filled with the same amount of LDH-Ca<sub>2</sub>Al were prepared using the same method as the blank control group. Table 1 provides the formulation of FKM/GO/LDH-Ca<sub>2</sub>Al composites. Different portions of GO/LDH-Ca<sub>2</sub>Al-filled fluoroelastomers were denoted as FKM/GO/LDH-Ca<sub>2</sub>Al-*x*, where *x* refers to the number of portions of nanofillers in 100 phr of fluoroelastomers.

**Table 1.** FKM nanocomposites formulation.

Samples	FKM 246	LUPEROX 101XL-50	TAIC	LDH-Ca <sub>2</sub> Al <sup>a</sup>	GO/LDH-Ca <sub>2</sub> Al <sup>a</sup>
FKM	100	5	5		
FKM/LDH-Ca <sub>2</sub> Al-5	100	5	5	5	5
FKM/LDH-Ca <sub>2</sub> Al-8	100	5	5	8	
FKM/LDH-Ca <sub>2</sub> Al-10	100	5	5	10	
FKM/GO/LDH-Ca <sub>2</sub> Al-5	100	5	5		5
FKM/GO/LDH-Ca <sub>2</sub> Al-8	100	5	5		8
FKM/GO/LDH-Ca <sub>2</sub> Al-10	100	5	5		10

<sup>a</sup> The densities of the materials FKM 246, LDH-Ca<sub>2</sub>Al, and GO/LDH-Ca<sub>2</sub>Al are 1.86, 1.65, and 2.01 g/cm<sup>3</sup>, respectively.

### 2.5. Characterization

Fourier transform infrared spectroscopy (FT-IR) measurements were carried out on a TENSOR II spectrometer (Bruker, MA, USA) at the wave number range of 4000–400 cm<sup>-1</sup> with a resolution of 4 cm<sup>-1</sup> and a 64-scan signal via the KBr pellet technique. An X-ray diffractometer (D8 Focus, Bruker) was used to characterize LDH-Ca<sub>2</sub>Al and GO/LDH-Ca<sub>2</sub>Al before and after CO<sub>2</sub> immersion and GO, and the measurements were carried out at a wavelength of  $\lambda = 0.154056$  nm with a step size of 0.01° under Cu/K $\alpha$  radiation. LDH-Ca<sub>2</sub>Al and GO/LDH-Ca<sub>2</sub>Al before and after CO<sub>2</sub> immersion, FKM/LDH-Ca<sub>2</sub>Al, and FKM/GO/LDH-Ca<sub>2</sub>Al were subjected to morphological observation by using a SU8010 cold field emission scanning electron microscope (SU8010, Hitachi, Japan). The CO<sub>2</sub> gas permeability of FKM/LDH-Ca<sub>2</sub>Al and FKM/GO/LDH-Ca<sub>2</sub>Al composites were measured via differential pressure by using a homemade gas permeability tester according to ISO 2782-1:2022 [32]. The samples to be tested were cut into dumbbell-shaped specimens. The tensile test was carried out by using a universal testing machine at room temperature with a tensile rate of 500 mm/min, following the GB/T 528–2009 standard [33] and three

parallel specimens were used for each group of materials. According to the ISO 7619-1:2010 standard [34], the Shore A hardness of the composites was tested using an LX A-type hardness tester. The samples were subjected to DMA testing by using a DMA (NETZSCH 242 C) in tensile mode at the frequency of 10 Hz. Each sample was scanned in the range of  $-50\text{ }^{\circ}\text{C}$  to  $60\text{ }^{\circ}\text{C}$  at a heating rate of  $3\text{ }^{\circ}\text{C}/\text{min}^{-1}$ . The samples were subjected to thermogravimetric analysis (TGA) by using a Shimadzu DTG-60 thermogravimetric analyzer, and the weight of the test samples ranged from 8 mg to 10 mg. The samples were heated from  $25\text{ }^{\circ}\text{C}$  to  $800\text{ }^{\circ}\text{C}$  at a heating rate of  $10\text{ }^{\circ}\text{C}/\text{min}$  under a nitrogen atmosphere purge of 100 mL/min. A differential scanning calorimeter (DSC, NETZSCH-5) was used to characterize the LDH- $\text{Ca}_2\text{Al}$  and GO/LDH- $\text{Ca}_2\text{Al}$  thermal transition. The weight of the test samples ranged from 6 mg to 10 mg and was heated from  $25\text{ }^{\circ}\text{C}$  to  $250\text{ }^{\circ}\text{C}$  at a heating rate of  $10\text{ }^{\circ}\text{C}/\text{min}$  under a nitrogen atmosphere of 100 mL/min.

The crosslink density of FKM/LDH- $\text{Ca}_2\text{Al}$  and FKM/GO/LDH- $\text{Ca}_2\text{Al}$  was measured using the equilibrium dissolution method [27,35] according to the standard ASTM D6814-02 [36]. Approximately 0.2 g of the sample was placed in a sealed container containing 25 mL of acetone and held at  $25\text{ }^{\circ}\text{C}$  for 3 days, during which the acetone solvent was changed every 24 h. The mass of the swelling equilibrium was measured as  $m_s$  and dried in a blower oven at  $70\text{ }^{\circ}\text{C}$  for 16 h. Then, the weight of the dried rubber  $m_d$  was measured, and the density  $\rho_d$  was calculated. The crosslink density  $v_e$  was calculated as follows:

$$V_r = (m_d / \rho_d) / [m_d / \rho_d + (m_s - m_d) / \rho_s] \quad (1)$$

$$v_e = \frac{-[\ln(1 - V_r) + V_r + \chi_1 V_r^2]}{[V_1 (V_r^{1/3} - V_r) / 2]} \quad (2)$$

where  $V_r$  and  $\rho_s$  are the volume fraction of rubber and the density of the solvent (the density of acetone is  $0.79\text{ g}/\text{cm}^3$ ), respectively,  $V_1$  is the molar volume of acetone solvent ( $73.53\text{ cm}^3/\text{mol}$ ), and  $\chi_1$  is the interaction parameter of the polymer with the solvent, which is 0.358 in this case. According to the Bristow–Watson equation, the following expression can be obtained [37]:

$$\chi_1 = \beta_1 + \left( \frac{V_1}{RT} \right) (\delta_s - \delta_p)^2 \quad (3)$$

where  $\beta_1$  is the lattice constant (typically 0.34),  $R$  is the gas constant,  $T$  is the absolute temperature, and  $\delta_p$  and  $\delta_s$  are the solubility parameters of FKM and solvent acetone, respectively.

### 3. Results and Discussion

#### 3.1. Fourier Transform Infrared (FTIR) Spectroscopy

The IR spectra of GO, Al-GO, LDH- $\text{Ca}_2\text{Al}$ , GO/LDH- $\text{Ca}_2\text{Al}$ , S-LDH- $\text{Ca}_2\text{Al}$ , and S-GO/LDH- $\text{Ca}_2\text{Al}$  are shown in Figure 1. The broad and strong absorption peaks of the infrared spectra of GO near  $3381\text{ cm}^{-1}$  represent the O–H stretching vibrations in carboxyl and hydroxyl groups, and the peaks at  $1223$  and  $1733\text{ cm}^{-1}$  represent the out-of-plane bending vibrations of O–H in COOH and its C=O stretching vibrations [38,39]. Alkoxy (C–OH) stretching vibrations and hydroxyl deformation vibrations occurred at  $1052$  and  $1390\text{ cm}^{-1}$ , respectively [40], and while that at  $1620\text{ cm}^{-1}$  can be attributed to the conjugate bond of aromatic C=C–C=C [39]. The peaks of the C=O stretching vibration of COOH and O–H out-of-plane bending vibration of COOH on Al-GO disappeared, and the symmetric and antisymmetric peaks of  $\text{COO}^-$  appeared near  $1636$  and  $1458\text{ cm}^{-1}$  [41]. The O–H stretching vibration peaks of Al–OH and Ca–OH of LDH- $\text{Ca}_2\text{Al}$ , GO/LDH- $\text{Ca}_2\text{Al}$ , S-LDH- $\text{Ca}_2\text{Al}$ , and S-GO/LDH- $\text{Ca}_2\text{Al}$  appeared at  $3634$  and  $3474\text{ cm}^{-1}$ , respectively, the bending vibration of the interlayer  $\text{H}_2\text{O}$  molecule was observed at approximately  $1621\text{ cm}^{-1}$ , and the absorption peaks at  $787$ ,  $535$ , and  $434\text{ cm}^{-1}$ , which are below  $800\text{ cm}^{-1}$ , represent M–O vibrational peaks (M is Ca or Al) [18,41,42]. In the IR spectra of GO/LDH- $\text{Ca}_2\text{Al}$ , Al-GO peaks appeared at  $3741$  and  $1637\text{ cm}^{-1}$ , but these peaks appear to be blue-shifted, possibly

because of the positively charged nature on the LDH- $\text{Ca}_2\text{Al}$  layer and the presence of the electron-absorbing induced effect. The peaks at  $1733$  and  $1223\text{ cm}^{-1}$ , which represent  $\text{COOH}$ , disappeared from the infrared spectra of  $\text{GO/LDH-Ca}_2\text{Al}$  and  $\text{Al-GO}$ , while symmetric and antisymmetric telescopic vibrational peaks near  $1458$  and  $1636\text{ cm}^{-1}$  for  $\text{COO}^-$  appeared [41]. The symmetric and antisymmetric telescopic vibrational peaks of  $\text{COO}^-$  in the  $\text{GO/LDH-Ca}_2\text{Al}$  spectra also shifted to the high-frequency region, indicating the presence of a strong interaction between  $\text{GO}$  and  $\text{LDH-Ca}_2\text{Al}$ .

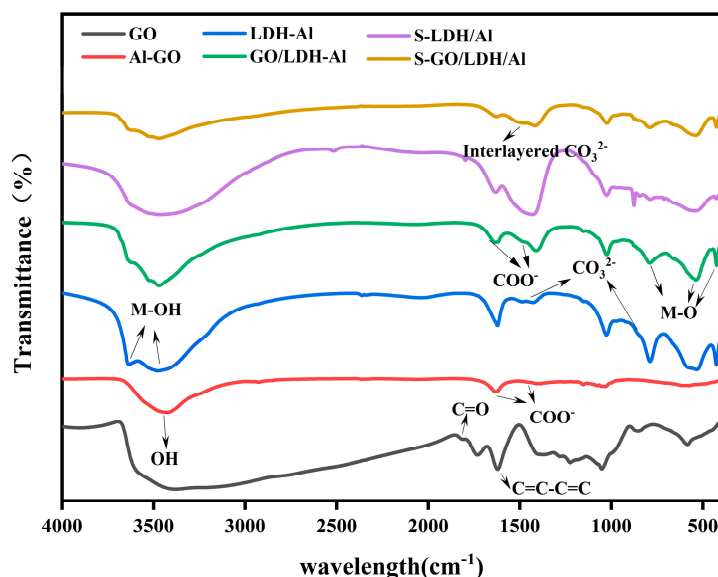


**Figure 1.** IR spectra of  $\text{GO}$ ,  $\text{Al-GO}$ ,  $\text{LDH-Ca}_2\text{Al}$ ,  $\text{GO/LDH-Ca}_2\text{Al}$ ,  $\text{S-LDH-Ca}_2\text{Al}$ , and  $\text{S-GO/LDH-Ca}_2\text{Al}$ .

The  $\text{CO}_3^{2-}$  peaks at  $1428$  and  $875\text{ cm}^{-1}$  represent small amounts of  $\text{CaCO}_3$  impurities in  $\text{GO/LDH-Ca}_2\text{Al}$  with  $\text{LDH-Ca}_2\text{Al}$  [43]. Both  $\text{LDH-Ca}_2\text{Al}$  and  $\text{GO/LDH-Ca}_2\text{Al}$  showed weak interlayer  $\text{CO}_3^{2-}$  absorption peaks at  $2974$  and  $1486\text{ cm}^{-1}$ , but the interlayer  $\text{CO}_3^{2-}$  absorption peaks of  $\text{LDH-Ca}_2\text{Al}$  of  $\text{S-LDH-Ca}_2\text{Al}$  and  $\text{S-GO/LDH-Ca}_2\text{Al}$  were significantly enhanced, suggesting that  $\text{CO}_2$  can be intercalated in the interlayer of  $\text{LDH-Ca}_2\text{Al}$  mainly in the form of  $\text{CO}_3^{2-}$  [18].

### 3.2. XRD Analysis of $\text{LDH-Ca}_2\text{Al}$ and $\text{GO/LDH-Ca}_2\text{Al}$

The XRD results of  $\text{GO}$ ,  $\text{LDH-Ca}_2\text{Al}$ , and  $\text{GO/LDH-Ca}_2\text{Al}$  are shown in Figure 2, where the appearance of  $\text{CaCO}_3$  impurity (PDF #97-001-6710 and PDF #97-018-1959) peaks proves the accuracy of the FTIR results (Figure 1). The X-ray diffraction pattern of  $\text{GO/LDH-Ca}_2\text{Al}$  (PDF#04-010-4677) does not show  $\text{GO}$  diffraction peaks, suggesting that the periodic stacking arrangement was not formed by the composite of  $\text{GO}$  and  $\text{LDH-Ca}_2\text{Al}$  [13]. The  $\text{GO/LDH-Ca}_2\text{Al}$  shows the typical Bragg reflection of  $\text{LDH-Ca}_2\text{Al}$  as the pristine  $\text{LDH-Ca}_2\text{Al}$ , but the diffraction peaks of  $\text{GO/LDH-Ca}_2\text{Al}$  at the (003) crystal plane shifted to a lower angle; according to Bragg equation ( $2d\sin(2\theta) = n\lambda$ ) the calculated  $\text{LDH-Ca}_2\text{Al}$  and  $\text{GO/LDH-Ca}_2\text{Al}$  basal spacings were approximately  $2.587$  and  $2.623\text{ nm}$ , respectively, and the thickness of the LDH-like hydromagnesite layer was  $0.48\text{ nm}$  [41]. The  $\text{LDH-Ca}_2\text{Al}$  and  $\text{GO/LDH-Ca}_2\text{Al}$  interlayer spacings were  $2.107$  and  $2.143\text{ nm}$ , respectively. Consequently,  $\text{Al-GO}$  formed a complex with  $\text{LDH-Ca}_2\text{Al}$ , resulting in an increase in interlayer spacing  $\text{CO}_2$  by approximately  $0.036\text{ nm}$ , as shown in Figure 2b. This phenomenon can be attributed to the strong interactions between the  $\text{Al-GO}$  and the  $\text{LDH-Ca}_2\text{Al}$  layers, which weakened the electrostatic interactions of the anionic in the interlayer channel with the cationic on the layer, consistent with the FTIR results. Given the increase in  $\text{GO/LDH-Ca}_2\text{Al}$  layer spacing, the specific surface area also increased, which provided more active sites for  $\text{CO}_2$  molecular adsorption and increased the possibility of  $\text{CO}_2$  gas adsorption and intercalation.

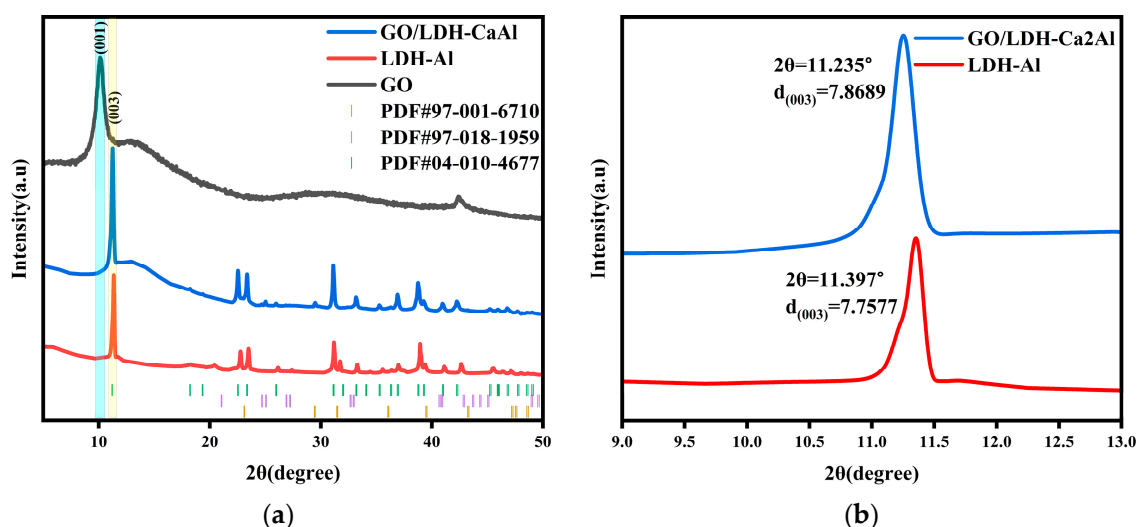


**Figure 2.** (a) XRD of GO, LDH- $\text{Ca}_2\text{Al}$ , and GO/LDH- $\text{Ca}_2\text{Al}$  and (b) localized enlargement near (003) of LDH- $\text{Ca}_2\text{Al}$  and GO/LDH- $\text{Ca}_2\text{Al}$ .

### 3.3. Structural Characteristics of LDH- $\text{Ca}_2\text{Al}$ and GO/LDH- $\text{Ca}_2\text{Al}$

The SEM of images of LDH- $\text{Ca}_2\text{Al}$  and GO/LDH- $\text{Ca}_2\text{Al}$  are shown in Figure 3. LDH- $\text{Ca}_2\text{Al}$  and GO/LDH- $\text{Ca}_2\text{Al}$  have obvious lamellar structures, and the diameter of LDH- $\text{Ca}_2\text{Al}$  flakes is in the range of 0.3–0.5  $\mu\text{m}$  with a thickness of approximately 0.03  $\mu\text{m}$ . The XRD of LDH- $\text{Ca}_2\text{Al}$  showed a layer spacing of approximately 2.107 nm (Figure 2), indicating that LDH- $\text{Ca}_2\text{Al}$  is composed of multilayered LDH- $\text{Ca}_2\text{Al}$  lamellae stacked along the (003) direction. In GO/LDH- $\text{Ca}_2\text{Al}$ , LDH- $\text{Ca}_2\text{Al}$  lamellae are much smaller than Al-GO (S1), which is consistent with the TEM results of GO/LDH- $\text{Ca}_2\text{Al}$  in Figure 4e. A closer look reveals that a large amount of LDH- $\text{Ca}_2\text{Al}$  is loaded onto the surface of Al-GO because of the existence of a strong interaction force between LDH- $\text{Ca}_2\text{Al}$  and Al-GO, which is consistent with the FITR results of GO/LDH- $\text{Ca}_2\text{Al}$  (Figure 1).

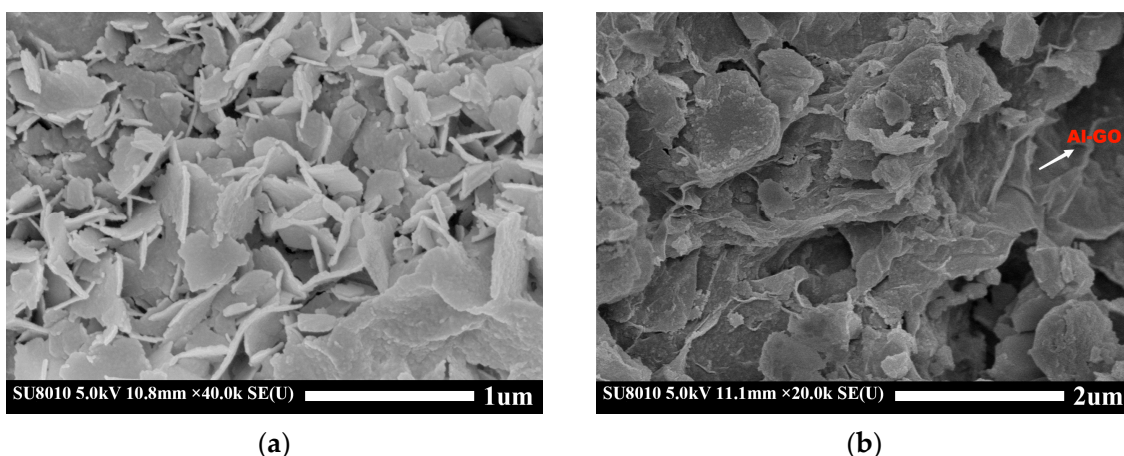


**Figure 3.** SEM images of (a) LDH- $\text{Ca}_2\text{Al}$  and (b) GO/LDH- $\text{Ca}_2\text{Al}$ .

The TEM of GO, LDH- $\text{Ca}_2\text{Al}$ , and GO/LDH- $\text{Ca}_2\text{Al}$  is shown in Figures S1 and 4, and they show a lamellar structure, which is consistent with the SEM results. The HR-TEM of LDH- $\text{Ca}_2\text{Al}$  in Figure 4d shows the appearance of obvious (110) and (104) lattice stripes, in which the spacing of the stripes are 0.286 and 0.378 nm, consistent with the results of (110) and (104) diffraction peaks in the XRD diffraction pattern. The SAED plot along the crystal axis (16, −7, 1) is shown in the lower right corner of Figure 4d, consistent with PDF#04-010-4677. A large amount of two-dimensional LDH- $\text{Ca}_2\text{Al}$  grows on GO/LDH- $\text{Ca}_2\text{Al}$ , and the HR-TEM of GO/LDH- $\text{Ca}_2\text{Al}$  clearly demonstrates that the two-dimensional

GO in GO/LDH- $\text{Ca}_2\text{Al}$  grows LDH- $\text{Ca}_2\text{Al}$  (Figure 4e); a (110) lattice face of LDH- $\text{Ca}_2\text{Al}$  was observed in the GO/LDH- $\text{Ca}_2\text{Al}$  lattice streak, and the SAED image in this region shows LDH- $\text{Ca}_2\text{Al}$  diffraction spots along the (17,16,2) directions [44], indicating that LDH- $\text{Ca}_2\text{Al}$  is deposited on the GO surface and stacked along the (003) direction on the GO surface.

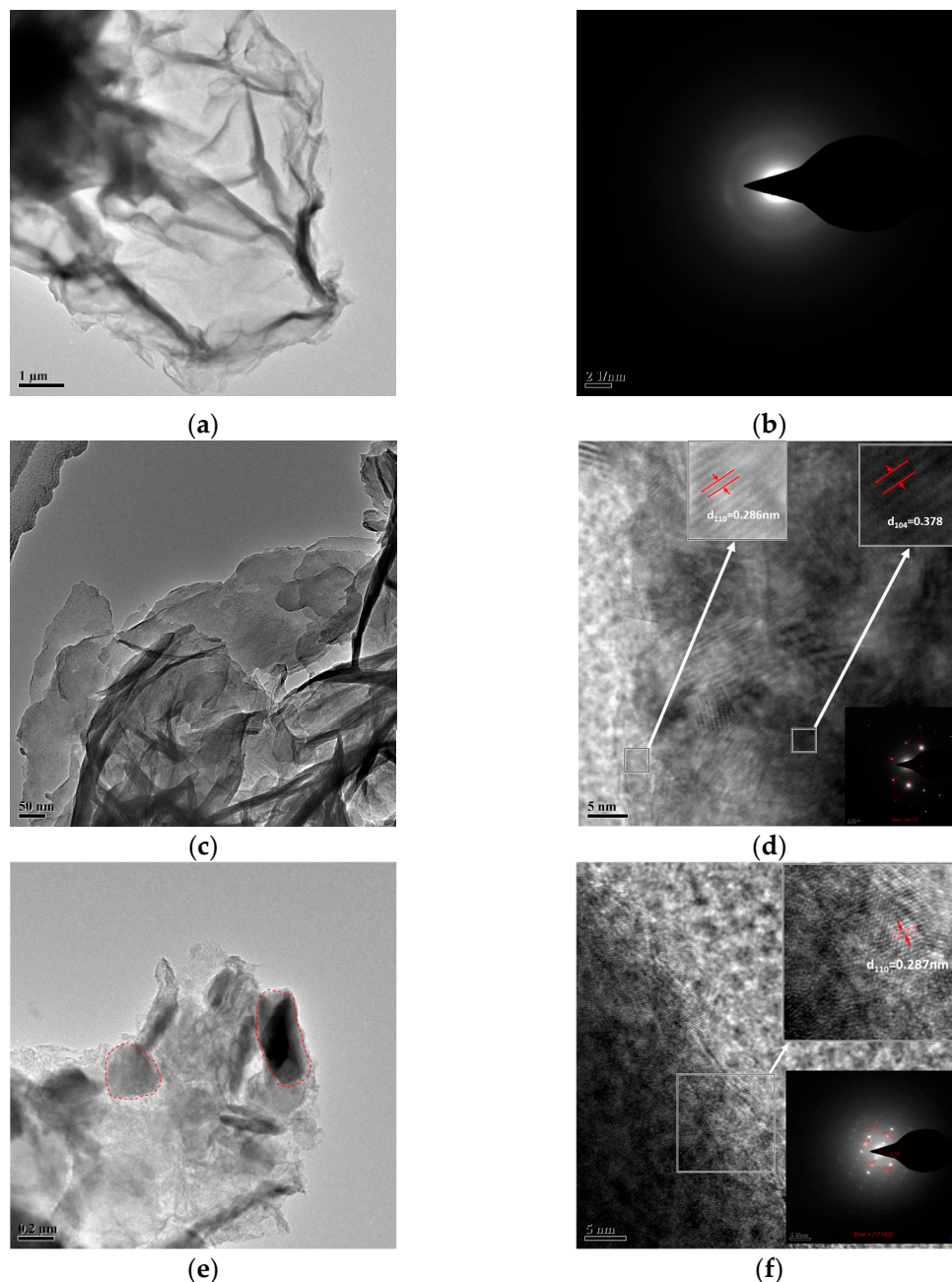


**Figure 4.** TEM of (a) GO, (c) LDH- $\text{Ca}_2\text{Al}$ , and (e) GO/LDH- $\text{Ca}_2\text{Al}$  (red circles—LDH- $\text{Ca}_2\text{Al}$ ), (b) SAED diagrams of GO, and (d) lattice fringes of LDH- $\text{Ca}_2\text{Al}$  and (f) GO/LDH- $\text{Ca}_2\text{Al}$  with SAED plots inset in the lower left corner.

### 3.4. Thermal Stability of GO, LDH- $\text{Ca}_2\text{Al}$ , and GO/LDH- $\text{Ca}_2\text{Al}$

The DSC and TGA curves of GO, LDH- $\text{Ca}_2\text{Al}$ , and GO/LDH- $\text{Ca}_2\text{Al}$  are shown in Figure 5a–c, respectively. Figure 5a shows a physisorbed water removal near 125.4, 136.4, and 117.5 °C for GO, LDH- $\text{Ca}_2\text{Al}$ , and GO/LDH- $\text{Ca}_2\text{Al}$ , respectively. Meanwhile, GO shows the oxidation of oxygen-containing functional groups near 198 °C, indicating an exothermic reaction [45]. The removal of interlayer  $\text{H}_2\text{O}$  molecules from LDH- $\text{Ca}_2\text{Al}$  and

GO/LDH-Ca<sub>2</sub>Al occurred near 192.6 and 200.3 °C, respectively, suggesting that GO/LDH-Ca<sub>2</sub>Al has better thermal stability than LDH-Ca<sub>2</sub>Al. Meanwhile, GO/LDH-Ca<sub>2</sub>Al did not show the exothermic reaction of GO near 198 °C, indicating that the thermal stability of GO in GO/LDH-Ca<sub>2</sub>Al was significantly improved due to the presence of strong interaction between Al-GO and LDH-Ca<sub>2</sub>Al.

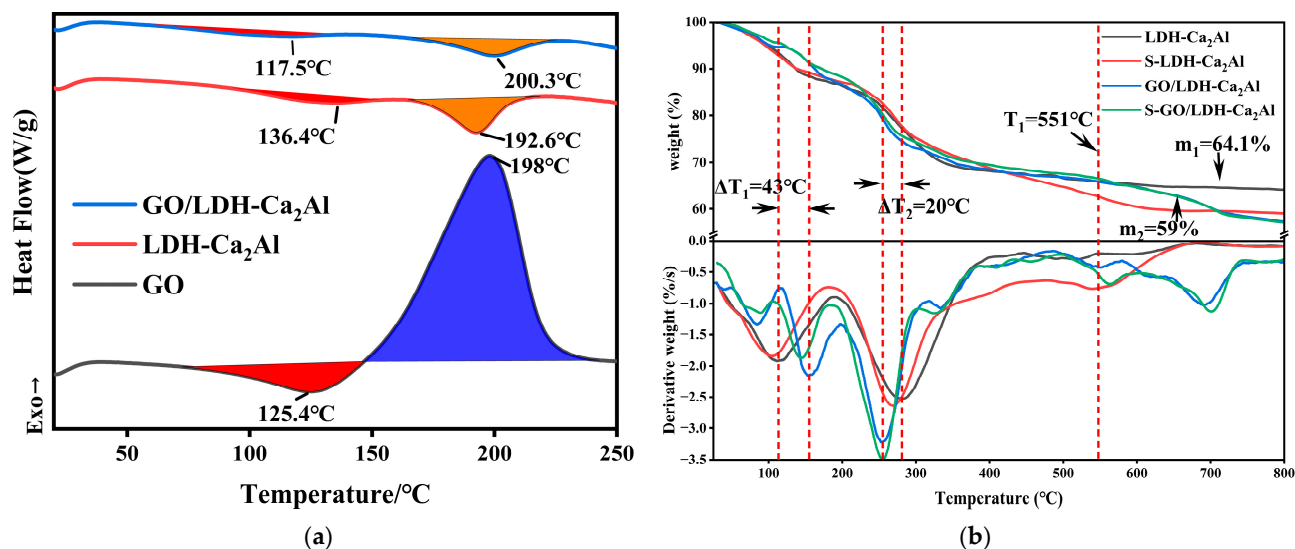


**Figure 5.** (a) DSC curves of GO, LDH-Ca<sub>2</sub>Al, and GO/LDH-Ca<sub>2</sub>Al and (b) TGA-DTG curves of LDH-Ca<sub>2</sub>Al, S-LDH-Ca<sub>2</sub>Al, GO/LDH-Ca<sub>2</sub>Al, and S-GO/LDH-Ca<sub>2</sub>Al.

The thermal stability of GO, LDH-Ca<sub>2</sub>Al, and GO/LDH-Ca<sub>2</sub>Al is also depicted in Figures S2 and 5b. Similar to the DSC results (Figure 5a), GO underwent three key weight loss steps at <125 °C corresponding to the removal of physically adsorbed water, 130–350 °C corresponding to the removal of oxygen functional groups, and 360–800 °C corresponding to the carbon framework of the oxidative pyrolysis [39]. Based on Figure 5b, three distinct weight loss steps can be observed for LDH-Ca<sub>2</sub>Al at 30–100 °C corresponding to the loss of physisorbed water, 100–170 °C corresponding to the process of interlayer water removal, 215–400 °C corresponding to the dehydroxylation of the layers and the removal of interlayer chloride ions, and 440–550 °C corresponding to the further elimination of the hydroxyl groups on the layers [18,41,46]. Compared with LDH-Ca<sub>2</sub>Al, the thermal stability of GO/LDH-Ca<sub>2</sub>Al was significantly improved between 30 and 200 °C. Although the temperature at which approximately 1.2% of physisorbed water was lost was approximately 7 °C lower than that of LDH-Ca<sub>2</sub>Al, the temperature at which the interlayer water was removed increased by nearly 43 °C ( $\Delta T_1$ ). Interestingly, the temperature of releasing interlayer chloride ions decreased by about 20 °C ( $\Delta T_2$ ), which was caused by the enlarged interlayer spacing of LDH-Ca<sub>2</sub>Al. At the same time, the thermal stability of the GO layer on GO/LDH-Ca<sub>2</sub>Al was improved, in which the carbon framework decomposition temperature increased by approximately 29 °C, respectively. The residual mass of S-LDH-Ca<sub>2</sub>Al with a value of approximately 59% at 800 °C ( $m_2$ ), which is approximately 5% higher than that of the LDH-Ca<sub>2</sub>Al, can be attributed to the decomposition of the carbonates that occurred after 450 °C based on the XRD patterns of S-LDH-Ca<sub>2</sub>Al; this finding revealed the presence of carbonates (Figure 6a) [18].

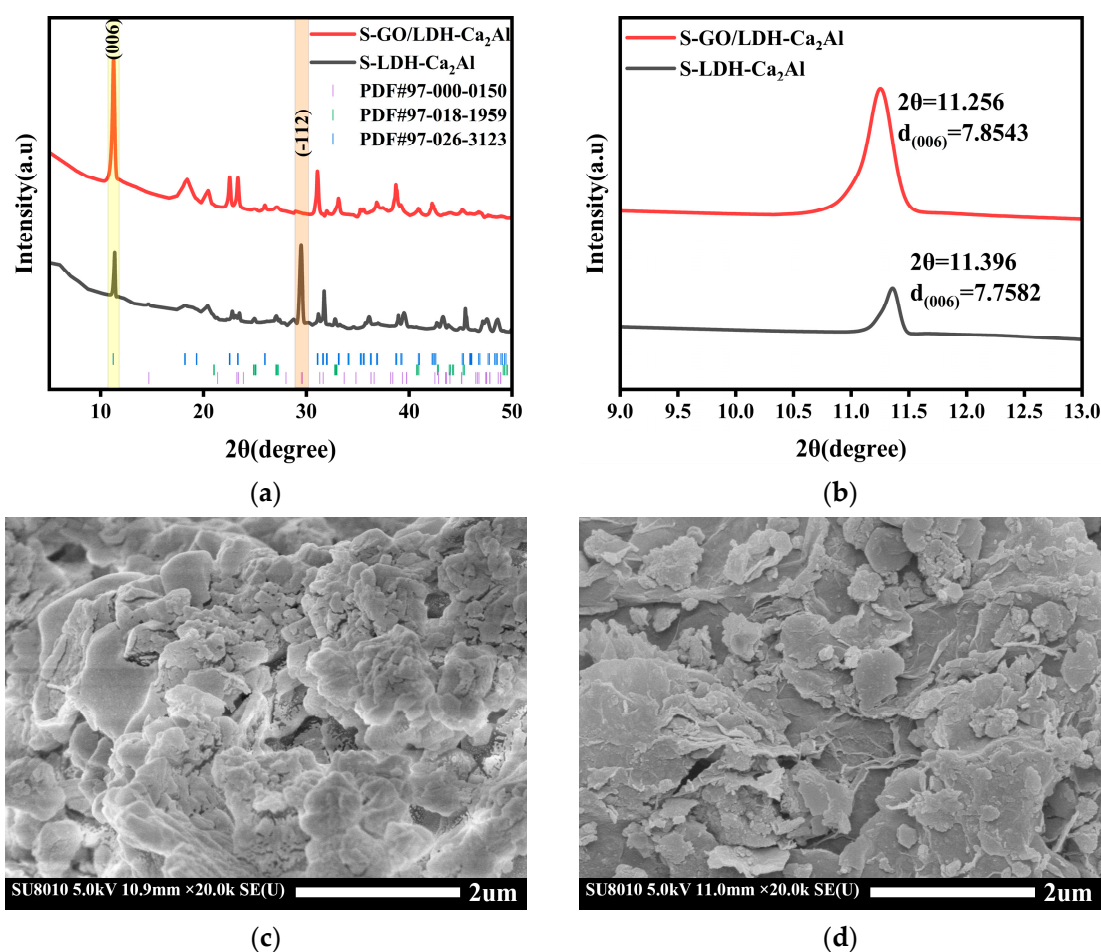


**Figure 6.** (a) XRD of S-LDH- $\text{Ca}_2\text{Al}$ , S-GO/LDH- $\text{Ca}_2\text{Al}$ , and (b) localized enlargement near (003) of LDH- $\text{Ca}_2\text{Al}$  and GO/LDH- $\text{Ca}_2\text{Al}$ . (c) SEM of S-LDH- $\text{Ca}_2\text{Al}$ , and (d) S-GO/LDH- $\text{Ca}_2\text{Al}$ .

### 3.5. Carbon Dioxide Resistance Stability of LDH- $\text{Ca}_2\text{Al}$ and GO/LDH- $\text{Ca}_2\text{Al}$

The XRD of S-LDH- $\text{Ca}_2\text{Al}$  and S-GO/LDH- $\text{Ca}_2\text{Al}$  are shown in Figure 6a,b. LDH- $\text{Ca}_2\text{Al}$  and GO/LDH- $\text{Ca}_2\text{Al}$  were placed in a pure  $\text{CO}_2$  environment at a pressure of 4 MPa and a temperature of 80 °C. After 1 day, the XRD diffraction peaks of the reaction products S-LDH- $\text{Ca}_2\text{Al}$  and S-GO/LDH- $\text{Ca}_2\text{Al}$  were very similar to those of  $\text{Ca}_4\text{Al}_2(\text{OH})_{12}(\text{OH}_{0.4}(\text{CO}_3)_{0.8}(\text{H}_2\text{O})_4)$  compounds (PDF#97-026-3123). According to the Bragg equation ( $2d\sin(2\theta) = n\lambda$ ), the calculated layer spacings of LDH- $\text{Ca}_2\text{Al}$ , GO/LDH- $\text{Ca}_2\text{Al}$ , S-LDH- $\text{Ca}_2\text{Al}$ , and S-GO/LDH- $\text{Ca}_2\text{Al}$  were 2.106, 2.143, 2.106, and 2.138 nm, respectively (Figures 2b and 6b) [41], and the kinetic diameter of  $\text{CO}_2$  was approximately 0.33 nm [47]. The IR spectra of S-LDH- $\text{Ca}_2\text{Al}$  and S-GO/LDH- $\text{Ca}_2\text{Al}$  also showed significant interlayer  $\text{CO}_3^{2-}$  absorption peaks (PDF #97-018-1959 and PDF #97-000-0150, Figure 1), suggesting that  $\text{CO}_2$  was intercalated into the interlayer of LDH and appeared in the interlayer in the form of  $\text{CO}_3^{2-}$ . The intensity of the  $\text{CaCO}_3$  diffraction peaks increased in the S-LDH- $\text{Ca}_2\text{Al}$ , and the micro-morphology of the S-LDH- $\text{Ca}_2\text{Al}$  showed a large number of massive structures (Figure 6c), indicating that  $\text{CO}_2$  reacted with LDH- $\text{Ca}_2\text{Al}$ , which led to an increase in  $\text{CO}_3^{2-}$  content in S-LDH- $\text{Ca}_2\text{Al}$ . By contrast, the intensity of the  $\text{CaCO}_3$  diffraction peaks in the XRD pattern of S-GO/LDH- $\text{Ca}_2\text{Al}$  decreased, no significant change was observed in the microscopic morphology (Figure 6d), and GO/LDH- $\text{Ca}_2\text{Al}$  hardly reacted with  $\text{CO}_2$ , indicating that GO/LDH- $\text{Ca}_2\text{Al}$  has a very good  $\text{CO}_2$ -resistant chemical stability, which is consistent with the TGA results (Figure 5). Table 2 also provides information on the change of  $\text{CaCO}_3$  content in LDH- $\text{Ca}_2\text{Al}$ , GO/LDH- $\text{Ca}_2\text{Al}$ , S-LDH- $\text{Ca}_2\text{Al}$ , and S-GO/LDH- $\text{Ca}_2\text{Al}$ .

**Table 2.** Contents of CaCO<sub>3</sub> in LDH-Ca<sub>2</sub>Al, GO/LDH-Ca<sub>2</sub>Al, S-LDH-Ca<sub>2</sub>Al, and S-GO/LDH-Ca<sub>2</sub>Al <sup>a</sup>.

Sample	Content (CaCO <sub>3</sub> ) (%)
LDH-Ca <sub>2</sub> Al	0.23
GO/LDH-Ca <sub>2</sub> Al	5.97
S-LDH-Ca <sub>2</sub> Al	59.94
S-GO/LDH-Ca <sub>2</sub> Al	2.37

<sup>a</sup> XRD data of LDH-Ca<sub>2</sub>Al, GO/LDH-Ca<sub>2</sub>Al, S-LDH-Ca<sub>2</sub>Al, and S-GO/LDH-Ca<sub>2</sub>Al were obtained via fine-tuning by using FullProf 2023.2 software.

### 3.6. Interfacial Interactions of FKM Matrix with LDH-Ca<sub>2</sub>Al and GO/LDH-Ca<sub>2</sub>Al

The interaction between the nanofillers and the polymer matrix influences the dispersion state of the nanofillers in the polymer, thus remarkably affecting the gas barrier properties and mechanical properties of the nanocomplexes [48–50]. GO/LDH-Ca<sub>2</sub>Al nanofillers had an excellent dispersion state in the FKM/GO/LDH-Ca<sub>2</sub>Al nanocomposites, and the energy storage modulus of the FKM/GO/LDH-Ca<sub>2</sub>Al complexes substantially increased because of the existence of a good phase interface between the GO/LDH-Ca<sub>2</sub>Al nanofillers and the rubber matrix compared with the LDH-Ca<sub>2</sub>Al nanofillers (Figure 7a,b). This interfacial interaction will be quantitatively measured next using two-phase modeling [51]. The loss tangent relationship between the filler and the unfilled polymer matrix satisfies the following equation [27,51,52]:

$$\tan \delta = \frac{\tan \delta_m}{1 + 1.5B\varphi} \quad (4)$$

where  $\tan \delta_m$  and  $\tan \delta$  represent the tangent values of the filler and the unfilled polymer matrix,  $\varphi$  is the volume fraction of the filler, and  $B$  is a phenomenological interaction parameter, which can represent the strength of the interface interaction between the filler and the matrix; the larger the value of  $B$ , the stronger the interface interaction between the filler and the polymer matrix [27]. The  $\tan \delta_m$ ,  $\tan \delta$ ,  $T_g$ , and  $B$  values of FKM, FKM/LDH-Ca<sub>2</sub>Al-8, and FKM/GO/LDH-Ca<sub>2</sub>Al-8 are shown in Table 3. The loss tangent  $\tan \delta$  and  $T_g$  of FKM/GO/LDH-Ca<sub>2</sub>Al shifted toward high temperature, and the  $B$  value of FKM/GO/LDH-Ca<sub>2</sub>Al-8 is approximately 0.528, which is slightly higher than that of FKM/LDH-Ca<sub>2</sub>Al-8 by 0.041. This finding indicates that the interfacial interactions between GO/LDH-Ca<sub>2</sub>Al and the FKM matrix were enhanced compared with that of LDH-Ca<sub>2</sub>Al, thus hindering the movement of the molecular chain segments. This finding explains that the crosslink density of FKM/GO/LDH-Ca<sub>2</sub>Al is always higher than that of FKM/LDH-Ca<sub>2</sub>Al for the fluoroelastomer composites filled with the same content of fillers, as shown in Figure 8. The SEM images of FKM/LDH-Ca<sub>2</sub>Al-8 and FKM/GO/LDH-Ca<sub>2</sub>Al-8 are shown in Figure 7a,b. The results indicate a good phase interface between GO/LDH-Ca<sub>2</sub>Al and the rubber matrix, which is caused by the strong interfacial interaction between GO/LDH-Ca<sub>2</sub>Al and the fluoroelastomer matrix than that of LDH-Ca<sub>2</sub>Al.

**Table 3.** Phenomenological interaction parameter ( $B$ ),  $\tan \delta_m$ ,  $\tan \delta$ ,  $T_g$ , and  $\varphi$  of FKM, FKM/LDH-Ca<sub>2</sub>Al-8, and FKM/GO/LDH-Ca<sub>2</sub>Al-8.

Sample	$\tan \delta_m$	$\tan \delta$	$\varphi$ (%)	$B$	$T_g$ (°C)
FKM	1.480	-	-	-	3.3
FKM/LDH-Ca <sub>2</sub> Al-8	-	1.396	8.254	0.487	4.9
FKM/GO/LDH-Ca <sub>2</sub> Al-8	-	1.404	6.88	0.528	5.6

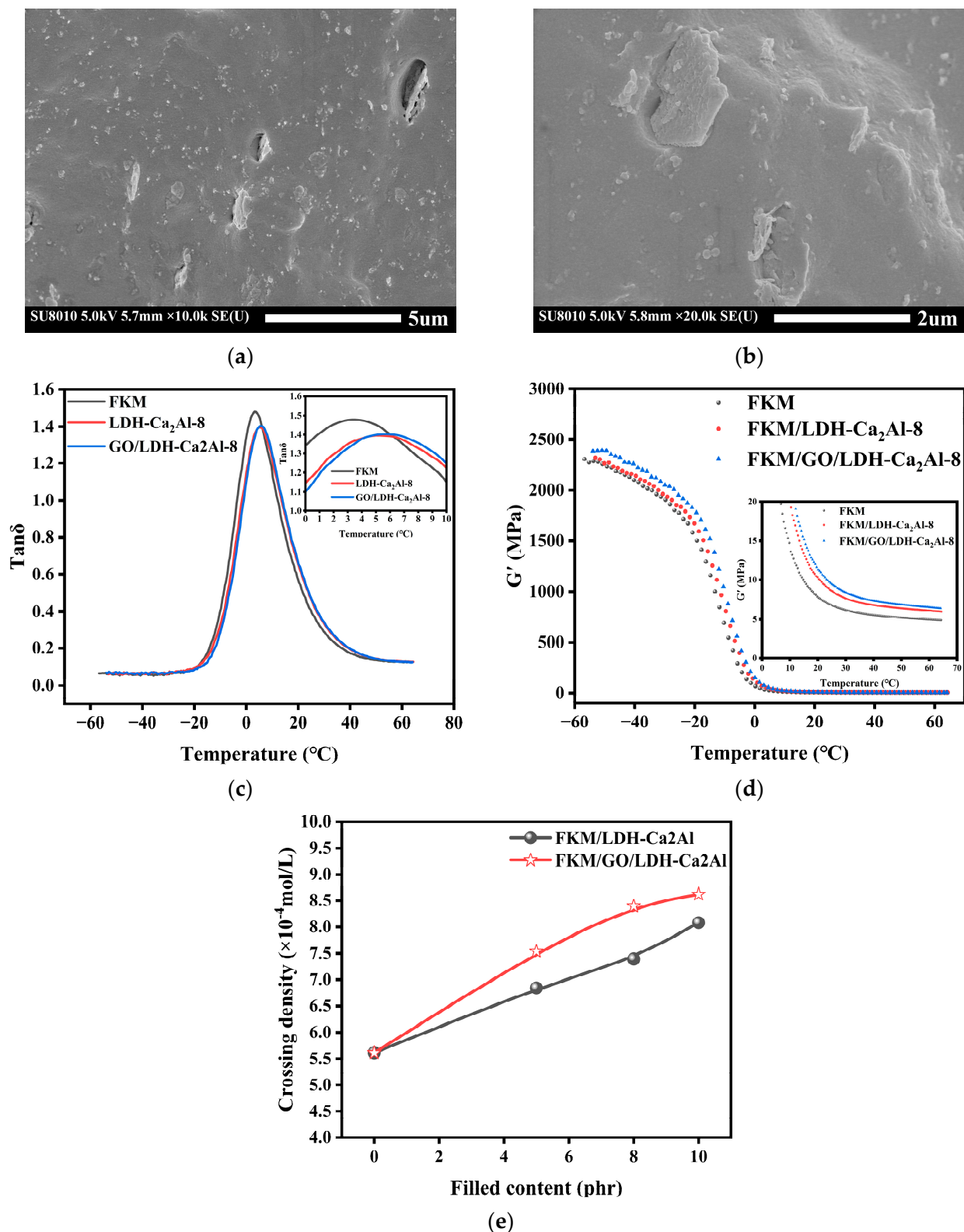


**Figure 7.** SEM images of (a) FKM/LDH-Ca<sub>2</sub>Al-8 and (b) FKM/GO/LDH-Ca<sub>2</sub>Al-8, (c,d) DMA of FKM, LDH-Ca<sub>2</sub>Al-8, and GO/LDH-Ca<sub>2</sub>Al-8, and (e) Crosslink density of FKM/LDH-Ca<sub>2</sub>Al and FKM/GO/LDH-Ca<sub>2</sub>Al with different filler parts.

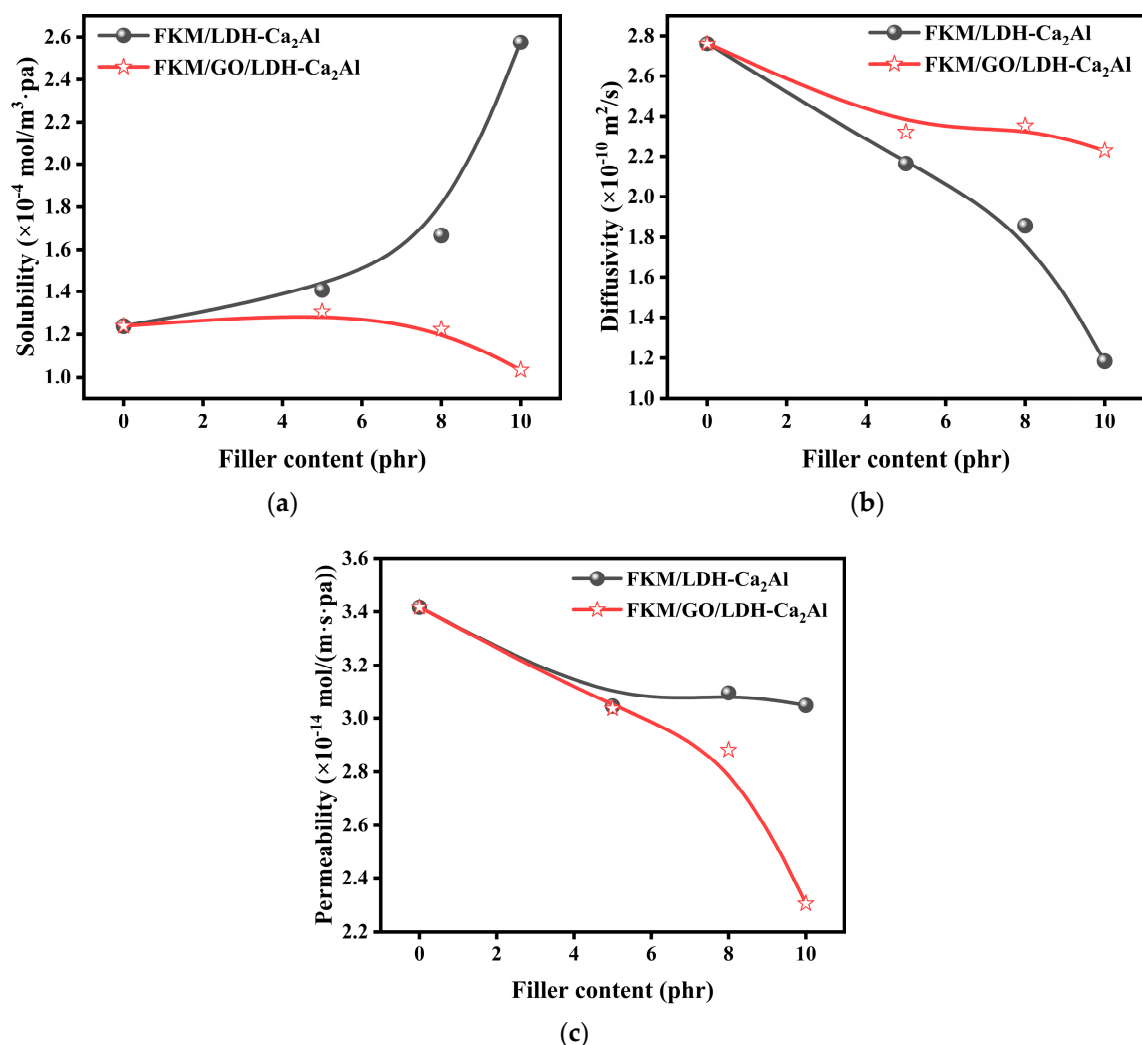


**Figure 8.** (a) Solubility ( $S$ ), (b) diffusion coefficient ( $D$ ), and (c) permeability coefficient ( $Q$ ) of FKM, FKM/GO/LDH-Ca<sub>2</sub>Al, and FKM/LDH-Ca<sub>2</sub>Al as a function of filler content.

### 3.7. Gas Barrier Properties of FKM/LDH-Ca<sub>2</sub>Al and FKM/GO/LDH-Ca<sub>2</sub>Al Composites

#### 3.7.1. Effect of Filler Content on the Gas Barrier Properties of FKM/LDH-Ca<sub>2</sub>Al and FKM/GO/LDH-Ca<sub>2</sub>Al Composites

The gas barrier properties of rubber composites, which were measured in terms of the gas permeability coefficient ( $Q = DS$ ), are related to the shape, content, and degree of dispersion of the filler [5,12,53], and lamellar fillers with large aspect ratios have good gas barrier properties [54]. LDH-Ca<sub>2</sub>Al and GO/LDH-Ca<sub>2</sub>Al are lamellar fillers with large aspect ratios (Figure 3a,b). The aspect ratios of LDH-Ca<sub>2</sub>Al are in the range of 10–16, and the  $Q$  and  $D$  of the rubber filled with 8 phr LDH-Ca<sub>2</sub>Al fillers were reduced by nearly 9% and 33%, respectively. The relationships of permeability coefficient ( $Q$ ), diffusion coefficient ( $D$ ), and solubility ( $S$ ) with the contents of LDH-Ca<sub>2</sub>Al and GO/LDH-Ca<sub>2</sub>Al are illustrated in Figure 8a–c. The results show that the permeability coefficients and diffusion coefficients of the rubber composites decrease significantly with the increase in filler content, which is consistent with the change in the crosslinking density of the rubber composites (Figure 7e). This phenomenon can be explained using the free volume theory [55,56]. The nanofillers can be approximated as physical cross-linking points and the cross-linking density increases with the increase in nanofiller content. The increase in cross-linking density shortens the distance between the rubber chains, reduces the mobility of the rubber chains, and leads to a decrease in the free volume fraction of the permeation path of the gas molecules [6]. The free volume fraction of the gas molecules' permeation path decreased.

The variation of solubility ( $S$ ) with filler content is given in Figure 8a. The solubility of FKM/LDH- $\text{Ca}_2\text{Al}$  increased significantly with the increase in LDH- $\text{Ca}_2\text{Al}$  content, and the solubility of the rubber composite increased by 108% when filled with 10 phr of LDH- $\text{Ca}_2\text{Al}$ . By contrast, the solubility of FKM/GO/LDH- $\text{Ca}_2\text{Al}$  gradually decreased with the increase in GO/LDH- $\text{Ca}_2\text{Al}$  content, and the solubility of the rubber composite decreased by about 19% when filled with 10 phr of GO/LDH- $\text{Ca}_2\text{Al}$ . This finding was obtained because LDH- $\text{Ca}_2\text{Al}$  is a nanofiller with high  $\text{CO}_2$  absorption [48]. Moreover, the loading of LDH- $\text{Ca}_2\text{Al}$  onto the GO surface reduces the content of exposed polar hydroxyl groups on the LDH- $\text{Ca}_2\text{Al}$  layer, thus forming strong hydrogen bonding interactions with O in the  $\text{CO}_2$  molecule and increasing the content of  $\text{CO}_2$  adsorbed on the surface of the filler. In addition, compared with the LDH- $\text{Ca}_2\text{Al}$ , the GO/LDH- $\text{Ca}_2\text{Al}$  in the composites has good compatibility (Figure 7a,b), which consistently supports the interfacial interactions between GO/LDH- $\text{Ca}_2\text{Al}$  and the rubber matrix (Table 3). Therefore, more constrained polymer regions are present near the interface between the rubber matrix and the filler [5,57], thus reducing the adsorption capacity of  $\text{CO}_2$  molecules at the interface.

Figure 8b shows the schematic relationship between filler content and diffusion coefficient, in which the diffusion coefficient of the rubber composites decreased significantly with the increase in the filler content of LDH- $\text{Ca}_2\text{Al}$  and GO/LDH- $\text{Ca}_2\text{Al}$ , which is consistent with many previous findings [5,58–61]. This finding was obtained because the filler increases the gas molecule diffusion path and hinders the gas molecule movement [6], while LDH- $\text{Ca}_2\text{Al}$  and GO/LDH- $\text{Ca}_2\text{Al}$  are multilayer fillers (Figures 2–4) with a layer spacing of more than 2.1 nm, which is significantly higher than the kinetic diameter of the  $\text{CO}_2$  molecule ( $\sim 0.33$  nm). Hence, the  $\text{CO}_2$  molecule can be interpolated into the layer spacing of the filler, thus significantly improving the gas molecule diffusion path. Accordingly, the diffusion coefficient of the rubber composite material was significantly reduced. Moreover, when the filler content of the filler reached 10 phr, the diffusion coefficient of the rubber composite material was reduced by nearly 57%. However, the diffusion coefficient of FKM/LDH- $\text{Ca}_2\text{Al}$  is lower than that of FKM/GO/LDH- $\text{Ca}_2\text{Al}$  at the same filler content, in which even the diffusion coefficient of FKM/LDH- $\text{Ca}_2\text{Al}$ -10 is approximately 47% lower than that of FKM/GO/LDH- $\text{Ca}_2\text{Al}$ -10. This finding was obtained because  $\text{CO}_2$  entered the spacing of the LDH- $\text{Ca}_2\text{Al}$  layers and reacted with the LDH- $\text{Ca}_2\text{Al}$  to generate inorganic compounds containing  $\text{CO}_3^{2-}$  (Table 2), such as  $\text{CaCO}_3$ . Consequently, the diffusion activation energy of  $\text{CO}_2$  gas remarkably decreased during diffusion in FKM/LDH- $\text{Ca}_2\text{Al}$  (Table 4). For example, the diffusion activation energy of FKM/LDH- $\text{Ca}_2\text{Al}$ -8 increased by approximately 27.6 J/mol. However, GO/LDH- $\text{Ca}_2\text{Al}$  has better-stabilizing properties during  $\text{CO}_2$  diffusion (Figures 2, 3b and 6), and the  $\text{CaCO}_3$  content of S-GO/LDH- $\text{Ca}_2\text{Al}$  did not change significantly compared with that of GO/LDH- $\text{Ca}_2\text{Al}$  (Table 2). Hence, although FKM/GO/LDH- $\text{Ca}_2\text{Al}$  lost some of the ability to reduce the diffusion coefficient brought by LDH- $\text{Ca}_2\text{Al}$ , it improved the  $\text{CO}_2$  resistance stability of FKM/GO/LDH- $\text{Ca}_2\text{Al}$ .

**Table 4.** Activation energy of D and S of FKM, FKM/LDH- $\text{Ca}_2\text{Al}$ -8, and FKM/GO/LDH- $\text{Ca}_2\text{Al}$ -8.

Sample	Activation Energy of D( $\Delta E$ ) <sup>a</sup>				Activation Energy of S( $\Delta H$ ) <sup>a</sup>			
	$D_0$ <sup>b</sup>	$\Delta E_{D0}$	$\Delta E_{Df}$	$\Delta E_{Dc}$	$S_0$ <sup>c</sup>	$\Delta H_{S0}$	$\Delta H_{sf}$	$\Delta H_{sc}$
FKM	$2.6 \times 10^{-2}$	−52.8	−	−	$1.8 \times 10^{-11}$	44.5	−	−
FKM/LDH- $\text{Ca}_2\text{Al}$ -8	$1.0 \times 10^{-6}$	−25.2	22.4	5.2	$2.2 \times 10^{-6}$	44.5	−32.2	−
FKM/GO/LDH- $\text{Ca}_2\text{Al}$ -8	$7.7 \times 10^{-6}$	−30.4	22.4	−	$4.7 \times 10^{-7}$	44.5	−32.2	3.8

<sup>a</sup> the unit of activation energy is KJ/mol. <sup>b</sup>  $D_0$  and <sup>c</sup>  $S_0$  are the dimensionless constants.

### 3.7.2. Effect of Temperature on the Gas Barrier Properties of FKM/LDH-Ca<sub>2</sub>Al and FKM/GO/LDH-Ca<sub>2</sub>Al Composites

The barrier mechanism of GO/LDH-Ca<sub>2</sub>Al and LDH-Ca<sub>2</sub>Al nanofillers in FKM/GO/LDH-Ca<sub>2</sub>Al with FKM/LDH-Ca<sub>2</sub>Al composites against CO<sub>2</sub> was investigated by conducting a temperature-dependence study on the gas barrier properties of FKM/LDH-Ca<sub>2</sub>Al and FKM/GO/LDH-Ca<sub>2</sub>Al composites. The permeability coefficients ( $Q$ ), diffusion coefficients ( $D$ ), and solubility ( $S$ ) of the rubber nanocomposites with temperature are given in Figure 9. The diffusion coefficients of FKM, FKM/GO/LDH-Ca<sub>2</sub>Al-8, and FKM/LDH-Ca<sub>2</sub>Al-8 remarkably increased with temperature, but the solubility remarkably decreased with the increase in temperature. Based on this phenomenon, the Arrhenius equation can be used to explain the relationship between the  $\ln(S)$  and  $\ln(D)$  of rubber nanocomposites and temperature ( $T$ ), which can be expressed by Equations (5) and (6) as follows:

$$\ln(S) = \ln(S_0) + \left( \Delta H_{S0} + \Delta H_{sf} + \Delta H_{sc} \right) / RT \quad (5)$$

$$\ln(D) = \ln(D_0) + \left( \Delta E_{D0} + \Delta E_{Df} + \Delta E_{Dc} \right) / RT \quad (6)$$

where  $S_0$  and  $D_0$  are pre-factor factors, which are related to the nature of the nanocomposites;  $\Delta H_{S0}$  and  $\Delta E_{D0}$  represent the heat of dissolution and diffusion activation energy of the pure polymer;  $\Delta H_{sf}$  and  $\Delta E_{Df}$  is the packing effect caused by nanofillers, which are related to the interaction of nanofillers with polymers and diffusion gases; and  $\Delta E_{Df}$  is related to factors such as the aspect ratio, size, and shape of the nanofiller. In this experiment,  $\Delta H_{sc}$  refers to the change in the heat of dissolution caused by the compound effect of GO and LDH-Ca<sub>2</sub>Al in GO/LDH-Ca<sub>2</sub>Al.  $\Delta E_{Dc}$  is the activation energy of the reaction between the nanofiller and the diffusion gas. Table 4 summarizes the relevant parameters of Equations (5) and (6) for the FKM, FKM/GO/LDH-Ca<sub>2</sub>Al-8, and FKM/LDH-Ca<sub>2</sub>Al-8 samples. The diffusion activation energy ( $\Delta E$ ) of the polymers is less than  $-25$  KJ/mol, and the solubility activation energy ( $\Delta H$ ) is higher than 12.3 KJ/mol, which is consistent with the diffusion coefficient ( $D$ ) and the solubility ( $S$ ) with temperature. The  $\Delta H_{sf}$  from the packing effect of LDH-Ca<sub>2</sub>Al is  $-32.2$  KJ/mol, resulting in a significant decrease in the heat of dissolution of CO<sub>2</sub> in the FKM/LDH-Ca<sub>2</sub>Al nanocomposites to approximately 12.3 KJ/mol, which explains the strong interaction between CO<sub>2</sub> and LDH-Ca<sub>2</sub>Al. This phenomenon led to an increase in the solubility of CO<sub>2</sub> in the FKM/LDH-Ca<sub>2</sub>Al nanocomposites. However, the change in the heat of dissolution caused by the compound effect of GO with LDH-Ca<sub>2</sub>Al ( $\Delta H_{sc}$ ) is 3.8 KJ/mol, which explains the existence of a strong interaction of GO/LDH-Ca<sub>2</sub>Al with the polymer matrix that reduced the CO<sub>2</sub> adsorption effect on the nanofiller surface. The diffusion activation energy of the nanocomposites remarkably increased, which rendered the activation energy of the reaction of CO<sub>2</sub> with GO/LDH-Ca<sub>2</sub>Al negligible, in which the value increased by approximately 42.5%. Hence, the diffusion coefficients of the FKM/LDH-Ca<sub>2</sub>Al and FKM/GO/LDH-Ca<sub>2</sub>Al nanocomposites were insensitive to the temperature variation. In addition to the packing effect caused by the filler ( $\Delta E_{Df}$ ), a chemical activation energy was observed between CO<sub>2</sub> and LDH-Ca<sub>2</sub>Al ( $\Delta E_{Dc} \approx 5.2$  KJ/mol) in the  $\Delta E$  of the FKM/LDH-Ca<sub>2</sub>Al nanocomposites. Therefore, it has a significantly lower diffusion coefficient than that of FKM/GO/LDH-Ca<sub>2</sub>Al. The permeability coefficient of the composites is a combination of the diffusion coefficient and solubility ( $Q = DS$ ) [5,48,62,63]. As shown in Figure 9c, the solubility of the nanocomposites substantially contributes to the permeability coefficient at 60–80 °C, resulting in the low permeability coefficient of FKM/GO/LDH-Ca<sub>2</sub>Al. By contrast, the diffusion coefficient of the nanocomposites substantially contributes to the permeability coefficient at 80–100 °C. Therefore, the permeability coefficient of the FKM/LDH-Ca<sub>2</sub>Al nanocomposites is lower than that of FKM/GO/LDH-Ca<sub>2</sub>Al.

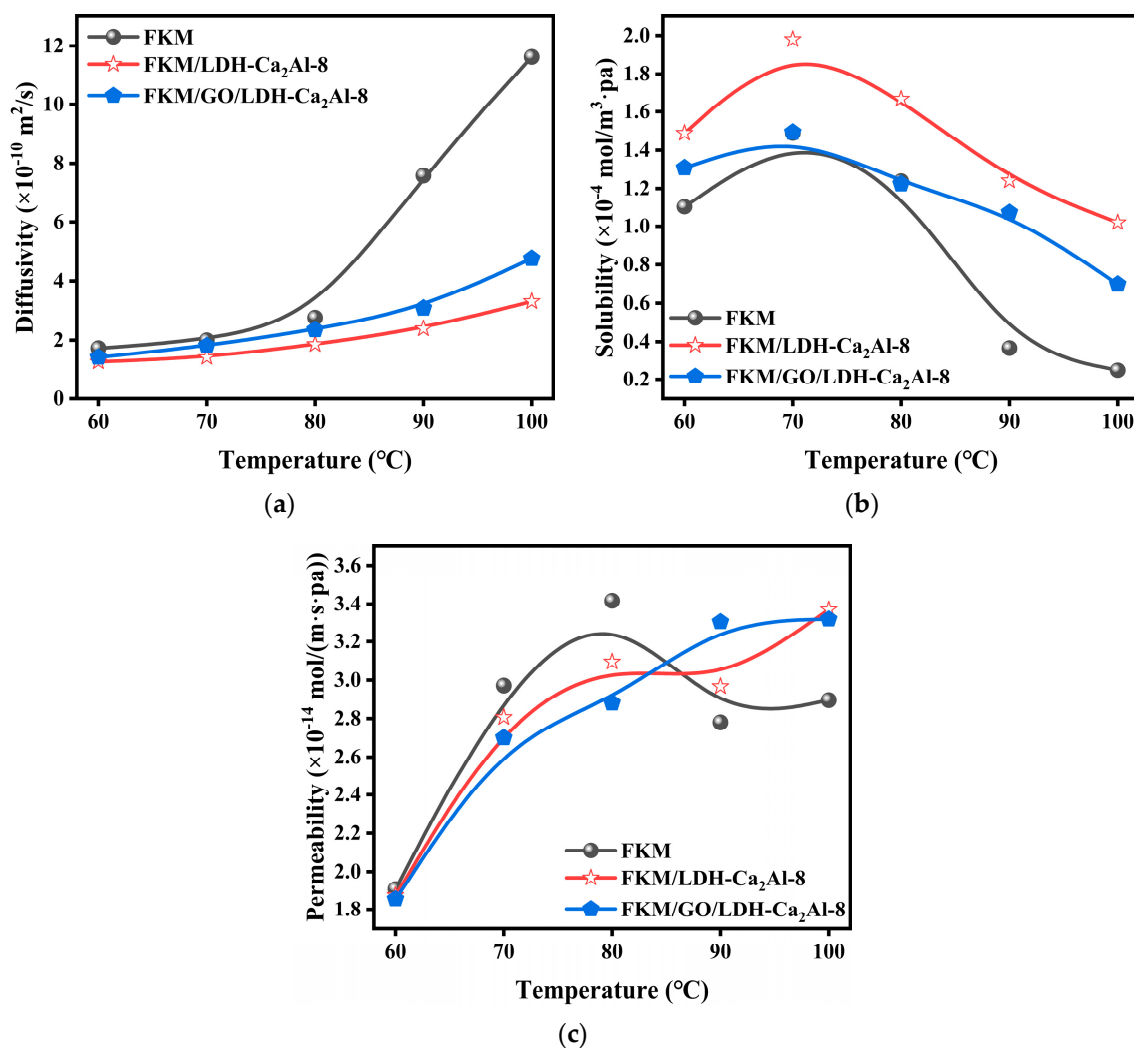


**Figure 9.** (a) Diffusion coefficients ( $D$ ), (b) solubility ( $S$ ), and (c) permeability coefficients ( $Q$ ) as a function of temperature for FKM, FKM/GO/LDH-Ca<sub>2</sub>Al-8, and FKM/LDH-Ca<sub>2</sub>Al-8.

### 3.8. Mechanical Properties of FKM/LDH-Ca<sub>2</sub>Al and FKM/GO/LDH-Ca<sub>2</sub>Al Nanocomposites

The effect of LDH-Ca<sub>2</sub>Al and GO/LDH-Ca<sub>2</sub>Al on the mechanical properties of fluoroelastomers was quantified by determining the key mechanical parameters of the nanocomposites with different filler contents (5, 8, and 10 phr), including 100% modulus ( $E_{100}$ ), Shore A hardness,  $\sigma_b$ , and  $\varepsilon_b$  (Figure 10 and Table 5). The mechanical properties of the nanocomposites were significantly improved compared with those of FKM, and interestingly, the  $\varepsilon_b$  of the nanocomposites gradually increased with the content of nanofillers, in which the largest  $\varepsilon_b$  ( $\varepsilon_b > 287\%$ ,  $\sigma_b > 11.1 \text{ MPa}$ ) value was obtained for the 10 phr filled FKM/GO/LDH-Ca<sub>2</sub>Al nanocomposites. This finding can be attributed to the orientation arrangement of the nanofillers with two-dimensional layered structures in the complexes when subjected to force, leading to the stable transfer of stress inside the material [9]. In addition, FKM/GO/LDH-Ca<sub>2</sub>Al nanocomposites exhibit superior mechanical properties to FKM/LDH-Ca<sub>2</sub>Al nanocomposites, in which  $\sigma_b$  and  $\varepsilon_b$  increased by approximately 25% and 12% (Table 5) because of the strong interfacial interaction between GO/LDH-Ca<sub>2</sub>Al and the polymer matrix, which promotes the efficient transfer of stress from the polymer matrix to GO/LDH-Ca<sub>2</sub>Al, consistent with the results described by the phenomenological interaction parameters (Table 3) [19].

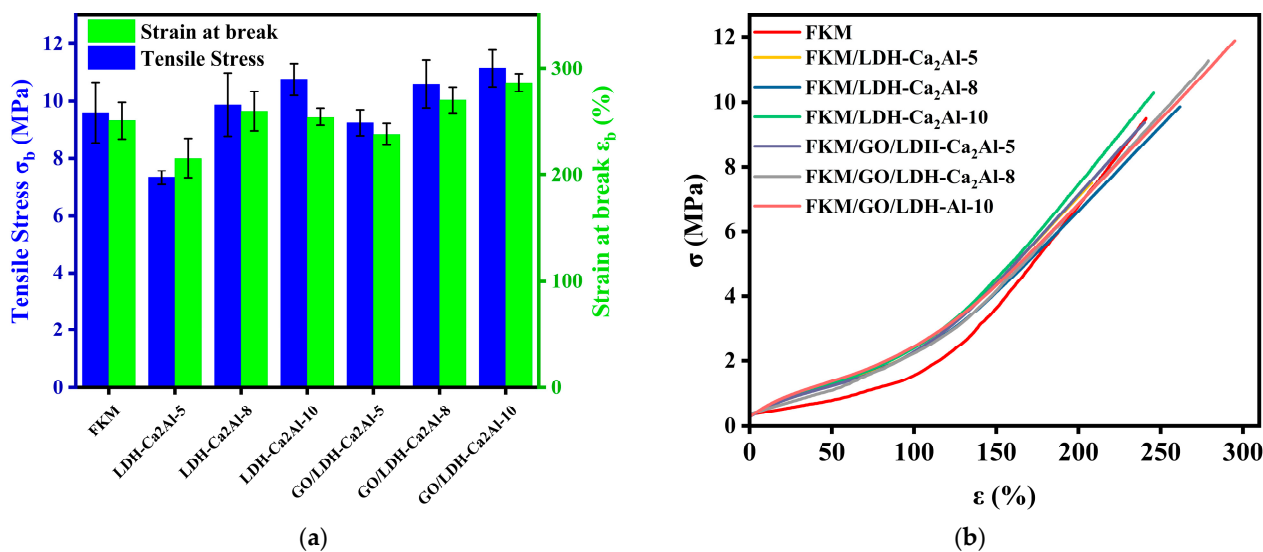


**Figure 10.** (a) Fracture strength ( $\sigma_b$ ) and strain ( $\epsilon_b$ ). (b) stress–strain curves of FKM, FKM/LDH-Ca<sub>2</sub>Al, and FKM/GO/LDH-Ca<sub>2</sub>Al nanocomposites.

**Table 5.** Mechanical properties of FKM, FKM/LDH-Ca<sub>2</sub>Al, and FKM/GO/LDH-Ca<sub>2</sub>Al complexes.

Sample	100% Modulus, $E_{100}$ (MPa)	Tensile Strength, $\sigma_b$ (MPa)	Strain at Break, $\epsilon_b$ (%)	Shore A Hardness
FKM	1.5 ± 0.1	9.6 ± 1.1	251 ± 17	50 ± 1
FKM/LDH-Ca <sub>2</sub> Al-5	2.1 ± 0.2	7.3 ± 0.2	215 ± 18	55 ± 1
FKM/LDH-Ca <sub>2</sub> Al-8	2.3 ± 0.08	9.9 ± 1.1	260 ± 19	56 ± 1
FKM/LDH-Ca <sub>2</sub> Al-10	2.4 ± 0.03	10.8 ± 0.6	254 ± 8	58 ± 1
FKM/GO/LDH-Ca <sub>2</sub> Al-5	2.3 ± 0.01	9.2 ± 0.5	238 ± 10	55 ± 1
FKM/GO/LDH-Ca <sub>2</sub> Al-8	2.2 ± 0.03	10.6 ± 0.8	270 ± 12	56 ± 1
FKM/GO/LDH-Ca <sub>2</sub> Al-10	2.4 ± 0.08	11.1 ± 0.6	287 ± 8	57 ± 1

#### 4. Conclusions

In this paper, the CO<sub>2</sub> gas barrier and mechanical properties of nanocomposites filled with Ca/Al layered hydroxide modified by GO (GO/LDH-Ca<sub>2</sub>Al) were investigated. The GO/LDH-Ca<sub>2</sub>Al nanocomposite filler was prepared by depositing LDH-Ca<sub>2</sub>Al on the surface of alkalized graphene oxide (Al-GO). This nanocomposite filler has good thermal stability compared with the pristine LDH-Ca<sub>2</sub>Al, and the temperature of the stripped interlayer water increased by nearly 43 °C. At the same time, its CO<sub>2</sub>-resistant stability was significantly improved, and almost no carbonate generation occurred at 80 °C and 4.3 MPa pure carbon dioxide environment, resulting in low CO<sub>2</sub> reactivity. The barrier mechanism of modified and unmodified LDH-Ca<sub>2</sub>Al-filled nanocomposites to carbon dioxide was also proposed, and the diffusion activation energy and solubility activation energy of the nanocomposites consisted of three components: (1)  $\Delta H_{S0}$  and  $\Delta E_{D0}$ , which were determined by the nature of the matrix; (2)  $\Delta H_{sf}$  and  $\Delta E_{Df}$  due to packing effect; and (3) the compound effect  $\Delta H_{sc}$  and reaction activation energy  $\Delta E_{Dc}$ . In the nanocomposites, the multilayer stacked LDH-Ca<sub>2</sub>Al acts as a CO<sub>2</sub> gas barrier to form a distorted diffusion path, and this effect induces an activation energy of  $\Delta E_{D0}$ . Considering the pro-CO<sub>2</sub> multilayer structure and strong chemical reactivity of LDH-Ca<sub>2</sub>Al, it provides the opportunity for CO<sub>2</sub> intercalation and reaction, resulting in the reaction activation energy of  $\Delta E_{Dc}$ . These two factors led to an increase in the diffusion activation energy of FKM/LDH-Ca<sub>2</sub>Al nanocomposites by approximately 42.5%. The solubility activation energy of FKM/GO/LDH-Ca<sub>2</sub>Al nanocomposites increased by approximately 3.8 kJ/mol compared with that of FKM/LDH-Ca<sub>2</sub>Al nanocomposites, which was caused by the compound effect of GO and LDH-Ca<sub>2</sub>Al. This phenomenon explains the existence

of strong interfacial interactions between GO/LDH-Ca<sub>2</sub>Al and the polymer matrix, thus reducing the CO<sub>2</sub> adsorption effect on the nanofiller surface. The permeability coefficients of the nanocomposites to CO<sub>2</sub> gradually decreased, and the mechanical properties (Shore A,  $\sigma_b$ , and  $\varepsilon_b$ ) were significantly improved with the increase in nanofiller content. The best CO<sub>2</sub> permeation resistance and mechanical properties were obtained for the FKM/GO/LDH-Ca<sub>2</sub>Al nanocomposites due to the strong interfacial interactions between GO/LDH-Ca<sub>2</sub>Al and FKM.

**Supplementary Materials:** The following supporting information can be downloaded at <https://www.mdpi.com/article/10.3390/polym15204151/s1>. Figure S1: SEM images of GO; Figure S2: TGA-DTG curves of GO.

**Author Contributions:** C.C.: Conceptualization, Formal analysis, Investigation, Resources, Writing—Review and Editing. D.P.: Methodology, Visualization, Investigation, Validation, Writing—Original Draft. Q.L.: Visualization, Investigation. M.Y.: Visualization, Investigation. X.M.: Visualization, supervision. Q.Z.: Formal analysis, Writing—Review and Editing, Supervision. All authors have read and agreed to the published version of the manuscript.

**Funding:** This study was supported financially by the China National Key R&D Program “Key Technology Research on Non-metallic Non-bonded Flexible Mixing Pipe for Deep Sea Mining” (2022YFC2803700): Topic 2 “Research and Development of Key Materials for Non-metallic Flexible Mixing Pipe for Deep Sea Mining” (2022YFC2803702).

**Institutional Review Board Statement:** Not applicable.

**Data Availability Statement:** The data presented in this study are available on request from the corresponding author.

**Conflicts of Interest:** The authors declare no conflict of interest.

## References

1. Moreira, D.; Pires, J.C.M. Atmospheric CO<sub>2</sub> capture by algae: Negative carbon dioxide emission path. *Bioresour. Technol.* **2016**, *215*, 371–379. [[CrossRef](#)] [[PubMed](#)]
2. Dai, Z.; Viswanathan, H.; Middleton, R.; Pan, F.; Ampomah, W.; Yang, C.; Jia, W.; Xiao, T.; Lee, S.Y.; McPherson, B.; et al. CO<sub>2</sub> Accounting and Risk Analysis for CO<sub>2</sub> Sequestration at Enhanced Oil Recovery Sites. *Environ. Sci. Technol.* **2016**, *50*, 7546–7554. [[CrossRef](#)]
3. Sethulekshmi, A.S.; Saritha, A.; Joseph, K. A comprehensive review on the recent advancements in natural rubber nanocomposites. *Int. J. Biol. Macromol.* **2022**, *194*, 819–842. [[CrossRef](#)]
4. Gent, A.N. Rubber Elasticity: Basic Concepts and Behavior. In *The Science and Technology of Rubber*; Academic Press: New York, NY, USA, 2013; pp. 1–26.
5. Guo, B.; Tang, Z.; Zhang, L. Transport performance in novel elastomer nanocomposites: Mechanism, design and control. *Prog. Polym. Sci.* **2016**, *61*, 29–66. [[CrossRef](#)]
6. Zhang, C.; An, X.; Tang, Z.; Fang, S.; Guo, B.; Zhang, L.; Liu, F.; Liu, J.; Chen, Z. Creation of Tortuosity in Unfilled Rubber via Heterogeneous Cross-Linking toward Improved Barrier Property. *Macromolecules* **2021**, *54*, 11522–11532. [[CrossRef](#)]
7. Pradhan, B.; Srivastava, S.K.; Bhowmick, A.K.; Saxena, A. Effect of bilayered stearate ion-modified Mg—Al layered double hydroxide on the thermal and mechanical properties of silicone rubber nanocomposites. *Polym. Int.* **2012**, *61*, 458–465. [[CrossRef](#)]
8. Laskowska, A.; Zaborski, M.; Boiteux, G.; Gain, O.; Marzec, A.; Maniukiewicz, W. Ionic elastomers based on carboxylated nitrile rubber (XNBR) and magnesium aluminum layered double hydroxide (hydrotalcite). *Express Polym. Lett.* **2014**, *8*, 374–386. [[CrossRef](#)]
9. Wang, X.; Zhang, Y.; Li, K.; Kang, Q.; He, Q. Study on the effect of layered double hydroxide on the mechanical and thermal properties of nitrile butadiene rubber. *J. Appl. Polym. Sci.* **2023**, *140*, e54257. [[CrossRef](#)]
10. Scherillo, G.; Lavorgna, M.; Buonocore, G.G.; Zhan, Y.H.; Xia, H.S.; Mensitieri, G.; Ambrosio, L. Tailoring assembly of reduced graphene oxide nanosheets to control gas barrier properties of natural rubber nanocomposites. *ACS Appl. Mater. Interfaces* **2014**, *6*, 2230–2234. [[CrossRef](#)]
11. Raef, M.; Razzaghi-Kashani, M. The role of interface in gas barrier properties of styrene butadiene rubber-reduced graphene oxide composites. *Polymer* **2019**, *182*, 121816. [[CrossRef](#)]
12. Wolf, C.; Angellier-Coussy, H.; Gontard, N.; Doghieri, F.; Guillard, V. How the shape of fillers affects the barrier properties of polymer/non-porous particles nanocomposites: A review. *J. Membr. Sci.* **2018**, *556*, 393–418. [[CrossRef](#)]

13. Mohd Sidek, H.B.; Jo, Y.K.; Kim, I.Y.; Hwang, S.-J. Stabilization of Layered Double Oxide in Hybrid Matrix of Graphene and Layered Metal Oxide Nanosheets: An Effective Way to Explore Efficient CO<sub>2</sub> Adsorbent. *J. Phys. Chem. C* **2016**, *120*, 23421–23429. [[CrossRef](#)]
14. Goh, K.H.; Lim, T.T.; Dong, Z. Application of layered double hydroxides for removal of oxyanions: A review. *Water Res.* **2008**, *42*, 1343–1368. [[CrossRef](#)]
15. Zhang, R.; Ai, Y.; Lu, Z. Application of Multifunctional Layered Double Hydroxides for Removing Environmental Pollutants: Recent Experimental and Theoretical Progress. *J. Environ. Chem. Eng.* **2020**, *8*, 103908. [[CrossRef](#)]
16. Sideris, P.J.; Nielsen, U.G.; Gan, Z.; Grey, C.P. Mg/Al ordering in layered double hydroxides revealed by multinuclear NMR spectroscopy. *Science* **2008**, *321*, 113–117. [[CrossRef](#)] [[PubMed](#)]
17. Lu, X.; Xue, H.; Gong, H.; Bai, M.; Tang, D.; Ma, R.; Sasaki, T. 2D Layered Double Hydroxide Nanosheets and Their Derivatives toward Efficient Oxygen Evolution Reaction. *Nanomicro. Lett.* **2020**, *12*, 86. [[CrossRef](#)] [[PubMed](#)]
18. Qu, J.; Zhong, L.; Li, Z.; Chen, M.; Zhang, Q.; Liu, X. Effect of anion addition on the syntheses of Ca–Al layered double hydroxide via a two-step mechanochemical process. *Appl. Clay Sci.* **2016**, *124–125*, 267–270. [[CrossRef](#)]
19. Zheng, L.; Jerrams, S.; Xu, Z.; Zhang, L.; Liu, L.; Wen, S. Enhanced gas barrier properties of graphene oxide/rubber composites with strong interfaces constructed by graphene oxide and sulfur. *Chem. Eng. J.* **2020**, *383*, 123100. [[CrossRef](#)]
20. Long, X.; Li, J.; Xiao, S.; Yan, K.; Wang, Z.; Chen, H.; Yang, S. A strongly coupled graphene and FeNi double hydroxide hybrid as an excellent electrocatalyst for the oxygen evolution reaction. *Angew. Chem. Int. Ed. Engl.* **2014**, *53*, 7584–7588. [[CrossRef](#)]
21. Jia, Y.; Zhang, L.; Gao, G.; Chen, H.; Wang, B.; Zhou, J.; Soo, M.T.; Hong, M.; Yan, X.; Qian, G.; et al. A Heterostructure Coupling of Exfoliated Ni-Fe Hydroxide Nanosheet and Defective Graphene as a Bifunctional Electrocatalyst for Overall Water Splitting. *Adv. Mater.* **2017**, *29*, 1700017. [[CrossRef](#)]
22. Chen, S.; Duan, J.; Jaroniec, M.; Qiao, S.Z. Three-dimensional N-doped graphene hydrogel/NiCo double hydroxide electrocatalysts for highly efficient oxygen evolution. *Angew. Chem. Int. Ed. Engl.* **2013**, *52*, 13567–13570. [[CrossRef](#)]
23. Mostovoy, A.S.; Yakovlev, A.V.; Lopukhova, M.I. Directional control of physico-chemical and mechanical properties of epoxide composites by the addition of graphite-graphene structures. *Polym.-Plast. Technol. Mater.* **2019**, *59*, 874–883. [[CrossRef](#)]
24. Wang, L.; Fu, W.; Peng, W. Enhanced strength and toughness of polyurethane rubber by introducing hydrogen bond sacrificial units at rubber-graphene interfaces. *Polym. Compos.* **2019**, *41*, 1242–1254. [[CrossRef](#)]
25. Li, J.; Zhang, P.; Chen, L.; Li, G.; Chen, H.; Jia, C.; Wu, Y.; Chen, M.; Zhao, X.; Song, P. Strong, tough and healable elastomer nanocomposites enabled by a hydrogen-bonded supramolecular network. *Compos. Commun.* **2020**, *22*, 100530. [[CrossRef](#)]
26. Zhou, S.; Liu, L.; Hu, S.; Wen, S. Properties of LDHs/ENR/SBR Gas Barrier Composites. *China Rubber Ind.* **2019**, *66*, 284. [[CrossRef](#)]
27. Rooj, S.; Das, A.; Heinrich, G. Tube-like natural halloysite/fluoroelastomer nanocomposites with simultaneous enhanced mechanical, dynamic mechanical and thermal properties. *Eur. Polym. J.* **2011**, *47*, 1746–1755. [[CrossRef](#)]
28. Silva, A.F.d.; Duarte, J.L.d.S.; Meili, L. Different routes for MgFe/LDH synthesis and application to remove pollutants of emerging concern. *Sep. Purif. Technol.* **2021**, *264*, 118353. [[CrossRef](#)]
29. Zhang, J.; Lin, Z.; Lan, Y.; Ren, G.; Chen, D.; Huang, F.; Hong, M. A multistep oriented attachment kinetics: Coarsening of ZnS nanoparticle in concentrated NaOH. *J. Am. Chem. Soc.* **2006**, *128*, 12981–12987. [[CrossRef](#)] [[PubMed](#)]
30. He, F.; Yang, Z.; Zhao, F.; Repo, E.; Yang, W.; Liao, Q.; Si, M.; Zou, B.; Lin, Z. Unveiling the dual roles of the intercalation of [MoS<sub>4</sub>]<sup>2-</sup> clusters in boosting heavy metal capture by Ca–Al layered double hydroxide. *Environ. Sci. Nano* **2023**, *10*, 190–202. [[CrossRef](#)]
31. Li, D.; Muller, M.B.; Gilje, S.; Kaner, R.B.; Wallace, G.G. Processable aqueous dispersions of graphene nanosheets. *Nat. Nanotechnol.* **2008**, *3*, 101–105. [[CrossRef](#)]
32. ISO 2782-1:2022; Rubber, Vulcanized or Thermoplastic—Determination of Permeability to Gases—Part 1: Differential-Pressure Methods. The International Organization for Standardization: Geneva, Switzerland, 2022.
33. GB/T 528-2009; Rubber, Vulcanized or Thermoplastic—Determination of Tensile Stress-Strain Properties. National Standards of the People's Republic of China: Beijing, China, 2009.
34. ISO 7619-1:2010; Rubber, Vulcanized or Thermoplastic—Determination of Indentation Hardness—Part 1: Durometer Method (Shore Hardness). The International Organization for Standardization: Geneva, Switzerland, 2010.
35. Yang, X.; Li, Q.; Li, Z.; Xu, X.; Liu, H.; Shang, S.; Song, Z. Preparation and Characterization of Room-Temperature-Vulcanized Silicone Rubber Using Acrylpimaric Acid-Modified Aminopropyltriethoxysilane as a Cross-Linking Agent. *ACS Sustain. Chem. Eng.* **2019**, *7*, 4964–4974. [[CrossRef](#)]
36. ASTM D6814-02; Standard Test Method for Determination of Percent Devulcanization of Crumb Rubber Based on Crosslink Density. ASTM: West Conshohocken, PA, USA, 2018. [[CrossRef](#)]
37. Sathi, S.G.; Jang, J.Y.; Jeong, K.U.; Nah, C. Thermally stable bromobutyl rubber with a high crosslinking density based on a 4,4'-bismaleimidodiphenylmethane curing agent. *J. Appl. Polym. Sci.* **2016**, *133*, 44092. [[CrossRef](#)]
38. Sarath, P.S.; Thomas, S.; Haponiuk, J.T.; George, S.C. Fabrication, characterization and properties of silane functionalized graphene oxide/silicone rubber nanocomposites. *J. Appl. Polym. Sci.* **2022**, *139*, e52299. [[CrossRef](#)]
39. Yap, P.L.; Kabiri, S.; Tran, D.N.H.; Losic, D. Multifunctional Binding Chemistry on Modified Graphene Composite for Selective and Highly Efficient Adsorption of Mercury. *ACS Appl. Mater. Interfaces* **2019**, *11*, 6350–6362. [[CrossRef](#)]

40. Costa, M.C.F.; Marangoni, V.S.; Ng, P.R.; Nguyen, H.T.L.; Carvalho, A.; Castro Neto, A.H. Accelerated Synthesis of Graphene Oxide from Graphene. *Nanomaterials* **2021**, *11*, 551. [[CrossRef](#)]
41. Jadam, M.L.; Syed Mohamad, S.A.; Zaki, H.M.; Jubri, Z.; Sarijo, S.H. Antibacterial activity and physicochemical characterization of calcium-aluminium-ciprofloxacin-layered double hydroxide. *J. Drug Deliv. Sci. Technol.* **2021**, *62*, 102314. [[CrossRef](#)]
42. Pérez-Barrado, E.; Pujol, M.C.; Aguiló, M.; Cesteros, Y.; Díaz, F.; Pallarès, J.; Marsal, L.F.; Salagre, P. Fast aging treatment for the synthesis of hydrocalumites using microwaves. *Appl. Clay Sci.* **2013**, *80–81*, 313–319. [[CrossRef](#)]
43. Santos, V.H.J.M.d.; Pontin, D.; Ponzi, G.G.D.; Stepanha, A.S.d.G.e.; Martel, R.B.; Schütz, M.K.; Einloft, S.M.O.; Dalla Vecchia, F. Application of Fourier Transform infrared spectroscopy (FTIR) coupled with multivariate regression for calcium carbonate (CaCO<sub>3</sub>) quantification in cement. *Constr. Build. Mater.* **2021**, *313*, 125413. [[CrossRef](#)]
44. Song, F.; Hu, X. Exfoliation of layered double hydroxides for enhanced oxygen evolution catalysis. *Nat. Commun.* **2014**, *5*, 4477. [[CrossRef](#)] [[PubMed](#)]
45. Mehetre, S.S.; Maktedar, S.S.; Singh, M. Understanding the mechanism of surface modification through enhanced thermal and electrochemical stabilities of N-doped graphene oxide. *Appl. Surf. Sci.* **2016**, *366*, 514–522. [[CrossRef](#)]
46. Zheng, L.; Xia, S.; Lu, X.; Hou, Z. Transesterification of glycerol with dimethyl carbonate over calcined Ca-Al hydrocalumite. *Chin. J. Catal.* **2015**, *36*, 1759–1765. [[CrossRef](#)]
47. Golemme, G.; Santaniello, A. Perfluoropolymer/Molecular Sieve Mixed-Matrix Membranes. *Membranes* **2019**, *9*, 19. [[CrossRef](#)] [[PubMed](#)]
48. Matteucci, S.; Kusuma, V.A.; Swinnea, S.; Freeman, B.D. Gas permeability, solubility and diffusivity in 1,2-polybutadiene containing brookite nanoparticles. *Polymer* **2008**, *49*, 757–773. [[CrossRef](#)]
49. Matteucci, S.; Kusuma, V.A.; Sanders, D.; Swinnea, S.; Freeman, B.D. Gas transport in TiO<sub>2</sub> nanoparticle-filled poly(1-trimethylsilyl-1-propyne). *J. Membr. Sci.* **2008**, *307*, 196–217. [[CrossRef](#)]
50. Merkel, T.C.; Freeman, B.D.; Spontak, R.J.; He, Z.; Pinnau, I.; Meakin, P.; Hill, A.J. Ultraporous, Reverse-Selective Nanocomposite Membranes. *Science* **2002**, *296*, 519–522. [[CrossRef](#)]
51. Song, K. Interphase characterization in rubber nanocomposites. In *Progress in Rubber Nanocomposites*; Elsevier: Amsterdam, The Netherlands, 2017; pp. 115–152.
52. He, S.-J.; Wang, Y.-Q.; Feng, Y.-P.; Liu, Q.-S.; Zhang, L.-Q. The preparation of an elastomer/silicate layer nanocompound with an exfoliated structure and a strong ionic interfacial interaction by utilizing an elastomer latex containing pyridine groups. *Nanotechnology* **2010**, *21*, 115601. [[CrossRef](#)]
53. Chen, H.; Li, Y.; Wang, S.; Li, Y.; Zhou, Y. Highly ordered structured montmorillonite/brominated butyl rubber nanocomposites: Dramatic enhancement of the gas barrier properties by an external magnetic field. *J. Membr. Sci.* **2018**, *546*, 22–30. [[CrossRef](#)]
54. Gatos, K.G.; Karger-Kocsis, J. Effect of the aspect ratio of silicate platelets on the mechanical and barrier properties of hydrogenated acrylonitrile butadiene rubber (HNBR)/layered silicate nanocomposites. *Eur. Polym. J.* **2007**, *43*, 1097–1104. [[CrossRef](#)]
55. Choudalakis, G.; Gotsis, A.D. Free volume and mass transport in polymer nanocomposites. *Curr. Opin. Colloid Interface Sci.* **2012**, *17*, 132–140. [[CrossRef](#)]
56. Srithawatpong, R.; Peng, Z.L.; Olson, B.G.; Jamieson, A.M.; Simha, R.; McGervey, J.D.; Maier, T.R.; Halasa, A.F.; Ishida, H. Positron annihilation lifetime studies of changes in free volume on cross-linking cis-polyisoprene, high-vinyl polybutadiene, and their miscible blends. *J. Polym. Sci. Part B Polym. Phys.* **1999**, *37*, 2754–2770. [[CrossRef](#)]
57. Beall, G. New conceptual model for interpreting nanocomposite behavior. In *Polymer–Clay Nanocomposites*; Wiley: Hoboken, NJ, USA, 2000; pp. 267–279.
58. Choudalakis, G.; Gotsis, A.D. Permeability of polymer/clay nanocomposites: A review. *Eur. Polym. J.* **2009**, *45*, 967–984. [[CrossRef](#)]
59. Jung, J.K.; Baek, U.B.; Lee, S.H.; Choi, M.C.; Bae, J.W. Hydrogen gas permeation in peroxide-crosslinked ethylene propylene diene monomer polymer composites with carbon black and silica fillers. *J. Polym. Sci.* **2023**, *61*, 460–471. [[CrossRef](#)]
60. Jung, J.K.; Lee, C.H.; Baek, U.B.; Choi, M.C.; Bae, J.W. Filler Influence on H<sub>2</sub> Permeation Properties in Sulfur-CrossLinked Ethylene Propylene Diene Monomer Polymers Blended with Different Concentrations of Carbon Black and Silica Fillers. *Polymers* **2022**, *14*, 592. [[CrossRef](#)] [[PubMed](#)]
61. Smith, A.P.; Crossley, S.D.; Gruber, T.C. Computational Investigation of the Effects of Spherical Filler Morphology and Loading on Diffusion Tortuosity and Rubber Permeability. *Rubber Chem. Technol.* **2013**, *86*, 175–189. [[CrossRef](#)]
62. Cui, Y.; Kundalwal, S.I.; Kumar, S. Gas barrier performance of graphene/polymer nanocomposites. *Carbon* **2016**, *98*, 313–333. [[CrossRef](#)]
63. Yoo, B.M.; Shin, H.J.; Yoon, H.W.; Park, H.B. Graphene and graphene oxide and their uses in barrier polymers. *J. Appl. Polym. Sci.* **2014**, *131*, 39628. [[CrossRef](#)]

**Disclaimer/Publisher’s Note:** The statements, opinions and data contained in all publications are solely those of the individual author(s) and contributor(s) and not of MDPI and/or the editor(s). MDPI and/or the editor(s) disclaim responsibility for any injury to people or property resulting from any ideas, methods, instructions or products referred to in the content.